REPORT DOCUMENTATION PAGE

Form Approved OMB NO. 0704-0188

1. REPORT DATE (DD-MM-YYYY)	2. REPORT TYPE	3. DATES COVERED (From - To)
13-01-2015	Final Report	25-Aug-2011 - 24-Aug-2013

4. TITLE AND SUBTITLE
Final Report: Acquisition of a Modified Suction Casting Instrument for the Fabrication of Radiation Tolerant Bulk nNanostructured Metallic Materials

5a. CONTRACT NUMBER
W911NF-11-1-0409

5b. GRANT NUMBER

5c. PROGRAM ELEMENT NUMBER
611103

6. AUTHORS
Xinghang Zhang

5d. PROJECT NUMBER

5e. TASK NUMBER

5f. WORK UNIT NUMBER

7. PERFORMING ORGANIZATION NAMES AND ADDRESSES
Texas Engineering Experiment Station
400 Harvey Mitchell Parkway South
Suite300
College Station, TX 77845 -4375

8. PERFORMING ORGANIZATION REPORT NUMBER

9. SPONSORING/MONITORING AGENCY NAME(S) AND ADDRESS (ES)
U.S. Army Research Office
P.O. Box 12211
Research Triangle Park, NC 27709-2211

10. SPONSOR/MONITOR'S ACRONYM(S)
ARO

11. SPONSOR/MONITOR'S REPORT NUMBER(S)
59201-MS-RIP.3

12. DISTRIBUTION AVAILIBILITY STATEMENT
Approved for Public Release; Distribution Unlimited

13. SUPPLEMENTARY NOTES
The views, opinions and/or findings contained in this report are those of the author(s) and should not contrued as an official Department of the Army position, policy or decision, unless so designated by other documentation.

14. ABSTRACT
This is the final progress report. The objective of this project is to acquire an instrument that enables the fabrication of bulk nanostructured metallic materials via a modified suction casting technique. The ultimate goal is to provide a platform that supports the design and fabrication of nanostructured metallic materials that have superior radiation tolerance. Specifically we will use the instrument to fabricate 1) multiphase bulk nanostructured metallic materials with high strength and ductility, and high temperature thermal stability; 2) nanoscale oxides dispersion strengthened (ODS) alloys.

15. SUBJECT TERMS
DURIP; suction casting system; final project report

16. SECURITY CLASSIFICATION OF:			17. LIMITATION OF ABSTRACT	15. NUMBER OF PAGES	19a. NAME OF RESPONSIBLE PERSON
a. REPORT	b. ABSTRACT	c. THIS PAGE			Xinghang Zhang
UU	UU	UU	UU		19b. TELEPHONE NUMBER: 979-845-2143

Report Title

Final Report: Acquisition of a Modified Suction Casting Instrument for the Fabrication of Radiation Tolerant Bulk nNanostructured Metallic Materials

ABSTRACT

This is the final progress report. The objective of this project is to acquire an instrument that enables the fabrication of bulk nanostructured metallic materials via a modified suction casting technique. The ultimate goal is to provide a platform that supports the design and fabrication of nanostructured metallic materials that have superior radiation tolerance. Specifically we will use the instrument to fabricate 1) multiphase bulk nanostructured metallic materials with high strength and ductility, and high temperature thermal stability; 2) nanoscale oxides dispersion strengthened (ODS) alloys.

The major technical accomplishments achieved during this project include the followings. First, we acquired an Edmund Buhler's Arc Melter Type AM machine with suction casting capability. The instrument is capable of melting a variety of high melting temperature metallic materials (up to 3,500oC), and perform rapid solidification via suction casting techniques. Second, we used this instrument to fabricate several bulk nanostructured metallic materials. In particular we fabricated bulk nanostructured Fe-Zr alloys via suction casting technique. The as-cast FeZr alloys have nanolaminates, and have extraordinary high temperature thermal stability. Finally we performed in situ radiation studies on the as-cast FeZr alloys have observed excellent radiation resistance in this nanostructured alloys.

Enter List of papers submitted or published that acknowledge ARO support from the start of the project to the date of this printing. List the papers, including journal references, in the following categories:

(a) Papers published in peer-reviewed journals (N/A for none)

Received Paper

TOTAL:

Number of Papers published in peer-reviewed journals:

(b) Papers published in non-peer-reviewed journals (N/A for none)

Received Paper

TOTAL:

Number of Papers published in non peer-reviewed journals:

(c) Presentations

Number of Presentations: 1.00

Non Peer-Reviewed Conference Proceeding publications (other than abstracts):

Received	Paper

TOTAL:

Number of Non Peer-Reviewed Conference Proceeding publications (other than abstracts):

Peer-Reviewed Conference Proceeding publications (other than abstracts):

Received	Paper

TOTAL:

Number of Peer-Reviewed Conference Proceeding publications (other than abstracts):

(d) Manuscripts

Received		Paper
01/13/2015	1.00	Z. Fan, , K.Y. Yu, , Y. Chen, , M. Song, , Y. Liu, , H. Wang, , M.A. Kirk, , M. Li , X. Zhang, . In situ Observation of Defect Annihilation in Kr Ion-Irradiated Bulk Fe/Amorphous-Fe2 Zr Nanocomposite Alloy, Materials Research letters (07 2014)
01/13/2015	2.00	Z. Fan, , J. Jian, , Y. Liu, , Y. Chen, , M. Song, , L. Jiao, , H. Wang, , X. Zhang. In situ studies on superior thermal stability of bulk FeZr nanolaminates, TBD (03 2015)

TOTAL: **2**

Number of Manuscripts:

Books

Received Book

TOTAL:

Received Book Chapter

TOTAL:

Patents Submitted

Patents Awarded

Awards

Gulf Oil/Thomas A. Dietz Career Development Professor

College of Engineering Holleran-Bowman Faculty Fellow award, 2014

TEES (Texas Engineering Experiment Station) fellow award, 2013.

Graduate Students

NAME	PERCENT_SUPPORTED	Discipline
Youxing Chen	0.00	
Zhe Fan	0.00	
FTE Equivalent:	**0.00**	
Total Number:	**2**	

Names of Post Doctorates

NAME	PERCENT_SUPPORTED
Kaiyuan Yu	0.00
FTE Equivalent:	**0.00**
Total Number:	**1**

Names of Faculty Supported

NAME	PERCENT_SUPPORTED	National Academy Member
Xinghang Zhang	0.00	
FTE Equivalent:	**0.00**	
Total Number:	**1**	

Names of Under Graduate students supported

NAME	PERCENT_SUPPORTED	Discipline
Rong Xu	0.00	Mechanical Engineering
FTE Equivalent:	**0.00**	
Total Number:	**1**	

Student Metrics

This section only applies to graduating undergraduates supported by this agreement in this reporting period

The number of undergraduates funded by this agreement who graduated during this period:	1.00
The number of undergraduates funded by this agreement who graduated during this period with a degree in science, mathematics, engineering, or technology fields:	1.00
The number of undergraduates funded by your agreement who graduated during this period and will continue to pursue a graduate or Ph.D. degree in science, mathematics, engineering, or technology fields:	1.00
Number of graduating undergraduates who achieved a 3.5 GPA to 4.0 (4.0 max scale):	1.00
Number of graduating undergraduates funded by a DoD funded Center of Excellence grant for Education, Research and Engineering:	0.00
The number of undergraduates funded by your agreement who graduated during this period and intend to work for the Department of Defense	0.00
The number of undergraduates funded by your agreement who graduated during this period and will receive scholarships or fellowships for further studies in science, mathematics, engineering or technology fields:	0.00

Names of Personnel receiving masters degrees

NAME
Total Number:

Names of personnel receiving PHDs

NAME
Kaiyuan Yu
Total Number: 1

Names of other research staff

NAME	PERCENT_SUPPORTED
FTE Equivalent:	
Total Number:	

Sub Contractors (DD882)

Inventions (DD882)

Scientific Progress

The major technical accomplishments achieved during this project include the followings. First, we acquired an Edmund Buhler's Arc Melter Type AM machine with suction casting capability. The instrument is capable of melting a variety of high melting temperature metallic materials (up to 3,500oC), and perform rapid solidification via suction casting techniques. Second, we used this instrument to fabricate several bulk nanostructured metallic materials. In particular we fabricated bulk nanostructured Fe-Zr alloys via suction casting technique. The as-cast FeZr alloys have nanolaminates, and have extraordinary high temperature thermal stability. Finally we performed in situ radiation studies on the as-cast FeZr alloys have observed excellent radiation resistance in this nanostructured alloys.

Technology Transfer

NA

Texas A&M University/Texas Engineering Experiment Station

Final Progress Report to ARO

on the W911NF1110409 Contract

"Acquisition of a Modified Suction Casting Instrument for the Fabrication of Radiation Tolerant Bulk nNanostructured Metallic Materials"

For the Period of Sep. 2011 – Sep. 2013

By

Xinghang Zhang, Texas A&M University

January 12, 2015

ABSTRACT

This is the final progress report. The objective of this project is to acquire an instrument that enables the fabrication of bulk nanostructured metallic materials via a modified suction casting technique. The ultimate goal is to provide a platform that supports the design and fabrication of nanostructured metallic materials that have superior radiation tolerance. Specifically we will use the instrument to fabricate 1) multiphase bulk nanostructured metallic materials with high strength and ductility, and high temperature thermal stability; 2) nanoscale oxides dispersion strengthened (ODS) alloys.

The major technical accomplishments achieved during this project include the followings. First, we acquired an Edmund Buhler's Arc Melter Type AM machine with suction casting capability. The instrument is capable of melting a variety of high melting temperature metallic materials (up to 3,500^{o}C), and perform rapid solidification via suction casting techniques. Second, we used this instrument to fabricate several bulk nanostructured metallic materials. In particular we fabricated bulk nanostructured Fe-Zr alloys via suction casting technique. The as-cast FeZr alloys have nanolaminates, and have extraordinary high temperature thermal stability. Finally we performed in situ radiation studies on the as-cast FeZr alloys have observed excellent radiation resistance in this nanostructured alloys.

Several papers have been published or to be submitted based on the support from this instrumentation. Two Ph.D. students worked on this instrumentation acquisition project and use the fabricated alloys for thermal stability and radiation stability studies. One of them becomes an assistant professor at a university.

1. Overall objective of the project

We aim to use the suction casting technique to fabricate bulk nanostructured metallic materials, and modify the technique by incorporating oxide nanoparticles so that we can fabricate bulk ODS alloys. To achieve this, we will need to 1) carefully select the composition of alloys; 2) control the cooling rate over a wide range; and 3) effectively incorporate oxide nanoparticles into liquid metals during casting and achieve homogeneity and reproducibility.

2. Description of acquired instrumentation

We procured the instrumentation fabricated by Edmund Buhler. The instrumentation fabricated by this company has received very positive recommendation by customers internationally and is the instrumentation we purchased has the following characteristics.

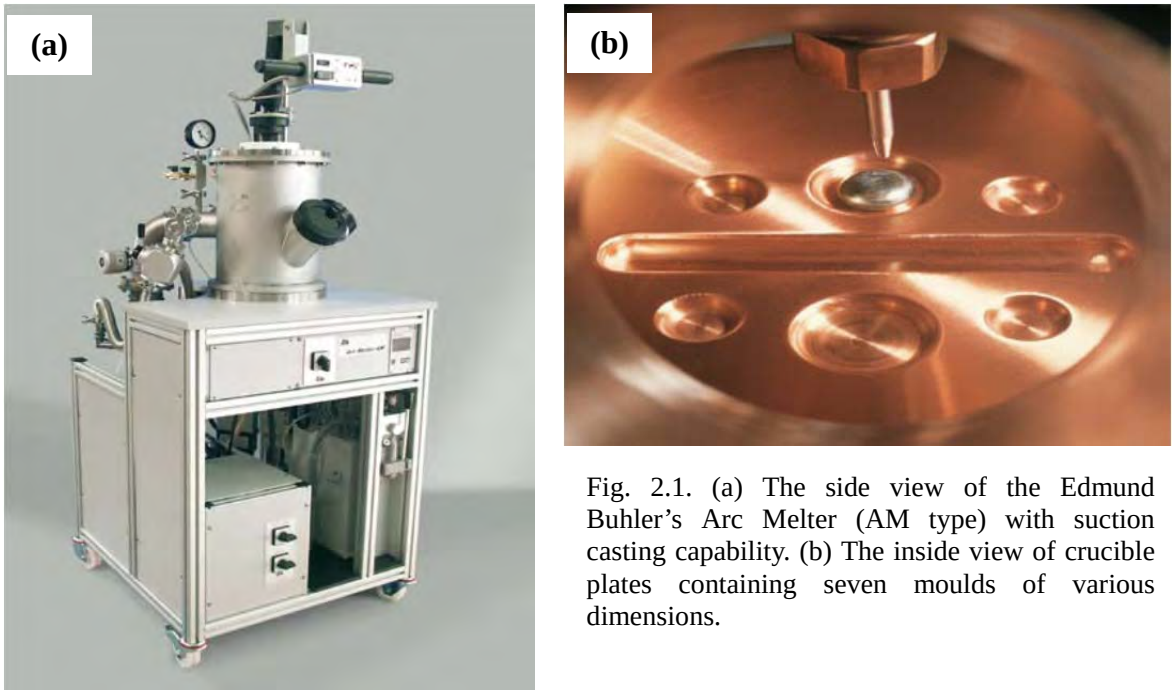

Fig. 2.1. (a) The side view of the Edmund Buhler’s Arc Melter (AM type) with suction casting capability. (b) The inside view of crucible plates containing seven moulds of various dimensions.

Edmund Buhler’s Arc Melter Type AM is designed to melt samples up to approximately 200 g at temperatures up to 3500 °C. A side view of the instrumentation is shown in Fig. 2.1a. The standard model is equipped with a high-vacuum pumping station, hydraulic heavy-duty hoist, motor-driven water-cooled tungsten electrode, and a crucible plate. The standard crucible plate consists of seven moulds: four ø 15 × 5 mm, two ø 30 × 5 mm, and one 110 × 10 × 7.5 mm, as shown in Fig. 1b.

The casting function consists of a rotatable crucible and an add-on ring to create space for customized moulds. The suction casting capability includes two-piece copper inserts for casting 150 mm long rods 3 and 5 mm in diameter, which require 8 and 23 g charges, respectively. Additionally, a heating/cooling coil surrounds the vacuum mould to influence the casting temperature. Also the suction casting option includes a water-cooled crucible plate with additional moulds for alloying before casting. In order to ensure homogeneity of alloys, the sample must be turned and remelted several times. In order to increase efficiency, Edmund Buhler offers a sample manipulator that may be used to turn samples in situ, without opening the chamber as shown in Fig. 2.2.

Fig. 2.2. Sample manipulator option for turning samples in-situ, without opening the chamber.

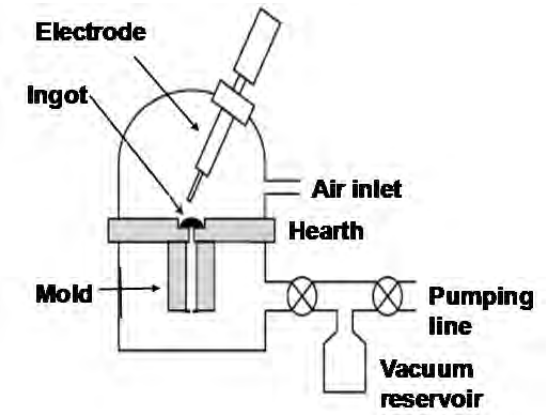

Fig. 2.3. Schematics of the key component of the suction casting technique and its operation principle.

Fig. 2.3 illustrates the operation principles of the suction casting technique. Basically raw materials with multiple components are mixed in a crucible in a chamber filled with UHP Ar. The lower chamber containing casting mold is connected to a multilevel vacuum system. After completely melt the metal mixtures by melting, the liquid metal is sucked into the mold by opening the gate valve in high vacuum chamber.

Modification of the suction casting technique – incorporate oxide nanoparticles into liquid metals to cast ODS alloys

This suction casting system provides us unique capabilities to fabricate bulk nanostructured metallic materials. However, it needs modification in order to incorporate oxide nanoparticles to fabricate ODS alloys. We modified the commercial system by adding an extra port through which a rotation load transfer arm can be inserted. A sample boat is attached to the end of the transfer arm. The boat is designed in such a away so that we can incorporate powders into the melted metals. We are in the process of testing this new design.

Installation and usage of the suction casting system

The system was installed in 2012 late summer in Materials Characterization Facility in Doherty 110. Figure 2.4 shows the panoramic view of the instrumentation and an undergraduate student, who has been trained in using this instrument. We have fabricated a variety of nanostructured alloy using this suction casting system.

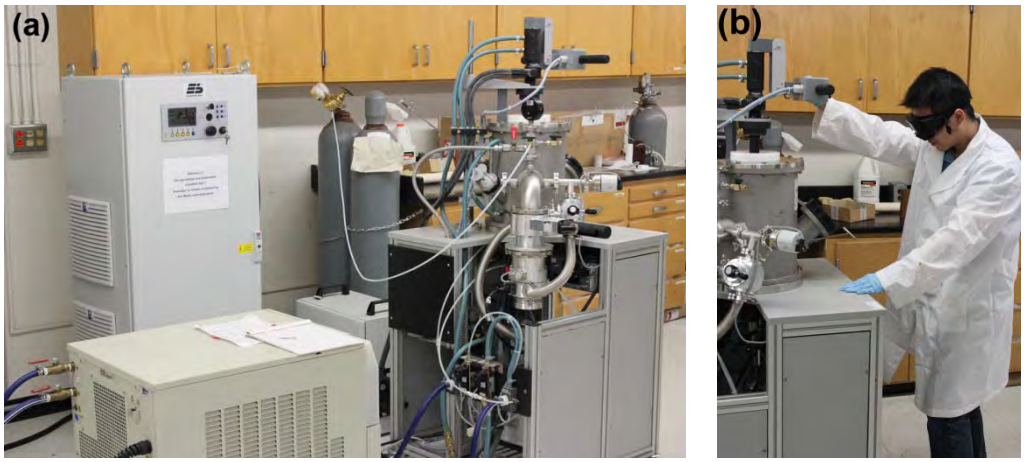

Fig. 2.4. (a) Panoramic view of the Edmund Buhler suction casting instrument. (b) An undergraduate student is being trained in using the suction casting instrument in the research facility.

3. Major technical accomplishments

3.1. *In situ* studies on superior thermal stability of bulk FeZr nanolaminates (To be submitted)

Abstract:

Nanostructured metals received significant attention due to their high mechanical strength. However, their poor thermal stability hinders their applications at high temperature. Here we show extraordinary thermal stability of FeZr nanocomposites with micron-sized Fe grains well distributed in the Fe/Fe_2Zr nanolaminates. The hardness of annealed FeZr nanocomposites remained unchanged up to 700^{o}C. Grain growth at higher annealing temperatures leads to hardness drop. Moreover, *in situ* annealing inside a transmission electron microscope revealed an unexpected coarsening mechanism of α-Fe grain: thermal stress arising from thermal expansion mismatch led to plastic yielding of large α-Fe grains. Debonding between α-Fe grain and Fe_2Zr along phase boundary introduced nanometer thick gaps surrounding the α-Fe grains, which were consequently refilled by diffusion of Fe from nanolaminates, manifested as grain coarsening.

3.1.1. Introduction

The pursuit of strong and thermally stable metallic materials has been an active research subject as such materials may have applications in extreme environments. Nanostructured metals usually contain high hardness, but relatively poor thermal stability than their coarse-grained counterparts. For instance, numerous nanocrystalline (nc) metals, such as Fe [1-3], Ni [4-7], and Cu [8-12], have high strength at room temperature, but upon annealing they typically soften because of rapid grain coarsening. Various strategies have been employed to enhance the thermal stability of nanostructured metals. Certain impurity once segregated to grain boundaries can reduce grain boundary energy and hence improve the thermal stability of nanograins [13, 14], and the inhomogenous solute distribution [15] can also enhance the thermal stability. The selection of solutes that can effectively enhance thermal stability of nc metals depends on parameters such as atomic size difference, solid solubility etc. Additionally, in tri-phase immiscible nanocomposites (TPIN), the growth of nanograins can be efficiently suppressed because of the immiscibility among each phase, the number of immiscible phases, and abundant triple junctions [16]. Meanwhile, nanotwinned (nt) metals have shown outstanding thermal stability. Because energy of coherent twin boundary is much lower than that of high angle grain boundaries, nanotwinned metals are thermodynamically more stable than nc counterparts [17-20]. Immiscible layer interface can also increase the thermal stability of nanolayered materials [21, 22]. Yet bulk nanolayered metallic materials are rarely synthesized or studied. This study

investigates the thermal stability of bulk Fe-Zr nanocomposites containing nanolaminates.

FeZr alloy, in many ways, is an interesting system. FeZr amorphous alloys can be used as good soft magnetic materials [23, 24], and they can be fabricated by melt-spinning [25], co-sputtering techniques and etc. [26, 27]. The incorporation of Zr into Fe by using ball-milling technique [28] leads to nc FeZr alloys with much higher hardness than pure nc Fe, and grain growth of nc FeZr alloys can be inhibited up to a relatively high temperature. Liu et al. [29] shows that FeZr alloy with eutectic composition exhibits outstanding compressive ductility, ~ 48% after annealing at 1190^{o}C for 48 h. The laves phase in steel with Zr [30] was shown to be stable close to its eutectic point. Radiation damage in FeZr alloys has also been studied for nuclear reactor applications [31-34]. Yu. et al shows that FeZr nanolaminates fabricated by rapid solidification have extraordinary radiation stability and tolerance. However, the thermal stability of these FeZr nanocomposites has not been well investigated [35]. Furthermore whether $Fe_{23}Zr_6$ is an equilibrium phase at room temperature is still under debate [36, 37].

To study the thermal stability of nanostructured FeZr, we applied suction casting technique to fabricate FeZr nanocomposite, which contains two components with different morphology: nearly equiaxed α-Fe grains and nanolaminates consisting of Fe and FeZr intermetallic nanolayers. *Ex situ* annealing studies show that the FeZr nanolaminate has extraordinary thermal stability. *In situ* annealing studies in a transmission electron microscope revealed that the grain coarsening in α-Fe grains at high temperature originates from thermal stress induced plastic yielding of α-Fe grains, followed by decohesion between α-Fe and FeZr along phase boundaries.

3.1.2. Methods and experiments

Alloy with a nominal composition of $Fe_{94.2}Zr_{5.8}$ was fabricated by acr-melting the mixture of high purity Fe (99.95%) and Zr (99.8%) under Zr-gettered ultrahigh purity (UHP) argon atmosphere using an Edmund Buhler Arc Melter. Cylindrical rods with a diameter of 3 mm and a length of 60 mm were prepared by suction casting via a water cooled copper mold. The alloy was melted at least 4 times before suction-casting to ensure the chemical homogeneity of the alloy. The chamber was evacuated to a based pressure better than 3×10^{-3} Pa and then inflated with UHP Argon to a pressure of 9×10^{4} Pa. A plate mold with the dimension of 2 × 25 × 50 mm was also used to fabricate the alloy. Thin slices of the alloy were cut from the cast alloys for

transmission electron microscopy (TEM) studies. The slices were mechanically polished to 50-100 μm and then electropolished by using 10% (at.) of perchloric acid and 90% (at.) of methanol. *In situ* heating experiment was performed on a JOEL 2010 transmission electron microscope operated at an accelerating voltage of 200 kV at a constant heating rate. A Gatan SC1000 Orius CCD camera (model 832) was used to record microstructure evolution during *in situ* annealing experiments. An FEI Tecnai G2 F20 microscope operated at 200 kV was also employed to study the microstructure and chemistry of cast alloys. Scanning transmission electron microscopy (STEM) and energy dispersive X-ray (EDX) analysis were conducted using Fischione ultra-high resolution high angle annular dark field (HADDF) detector (0.23 nm in the STEM image mode) and Oxford instruments detectors with a spatial resolution of ~1 nm attached to the Tecnai F20. Scanning electron microscopy (SEM) experiments were performed by using a Quanta 600 field emission scanning electron microscope. Hardness and elastic modulus of the specimens were determined by using instrumented nanoindentation technique on a Fischerscope 2000XYp nano/micro indentor. A minimum of 25 indents were used to obtain an average hardness value at various indentation depth. The hardness values were determined as the hardness plateau in the hardness vs. indentation depth plot [39, 40].

3.1.3. Results

The as-cast $Fe_{94.2}Zr_{5.8}$ alloy (by using the plate mould) shown in Fig. 1a contained two phases: α-Fe grains and nanolaminate matrix. The α-Fe grains are several microns in diameter. A high-magnification SEM image in Fig. 1b shows that the nanolaminate consists of alternating nanolayers of α-Fe and Fe_2Zr (laves phase). Besides large patches of straight nanolayers, cellular domains composed of α-Fe and Fe_2Zr were also observed. The α-Fe grains were typically separated from nanolaminates by Fe_2Zr nanolayers.

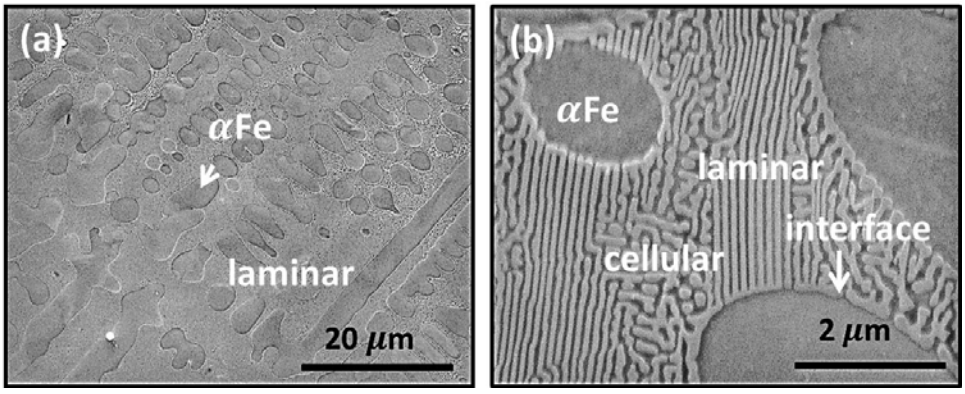

Figure 1. Microstructure of as-cast $Fe_{94.2}Zr_{5.8}$ nanocomposite prepared by suction casting method using a plate mould. (a) Low-magnification SEM image of cast $Fe_{94.2}Zr_{5.8}$ alloy. Nanolaminates matrix contained relatively large α-Fe grains with several microns in diameter. (b) High-magnification SEM images of the alloy consisting of regions of different morphology, including large α-Fe grains, cellular and laminar nanolayers. The typical interface between laminar (cellular) regions and α-Fe grains is marked.

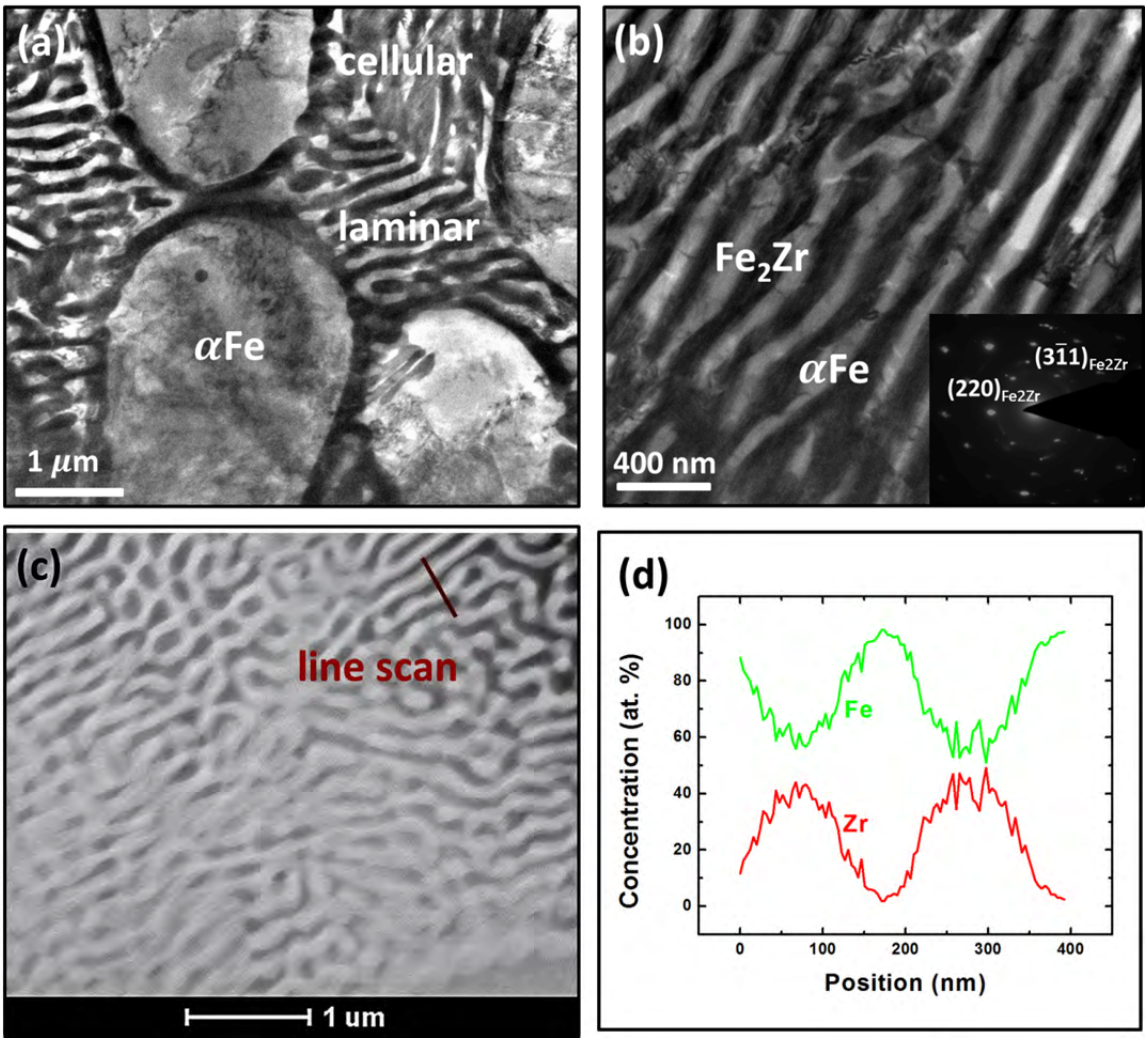

Figure 2. TEM images showing microstructure of $Fe_{94.2}Zr_{5.8}$ alloy prepared by suction casting using a plate mold. (a) Low magnification TEM image shows that the as-cast alloy contains three components: α-Fe grain, straight laminates and cellular phases. (b) Higher magnification TEM image showing straight laminates. The inserted selected area diffraction (SAD) pattern shows single crystal-like Fe_2Zr (C15) eutectic phase. The zone axis of Fe_2Zr is <114>. (c) Scanning transmission electron microcopy (STEM) shows the alternating laminates with ~ 100 nm layer thickness. (d) The EDS composition profiles show alternating Fe and Fe_2Zr nanolaminates.

A low-magnification TEM micrograph of the as-cast $Fe_{94.2}Zr_{5.8}$ nanocomposite (plate mould in Fig. 2a) shows the coexistence of α-Fe grains, cellular and laminar domains. Fig. 2b shows typical nanolaminates containing dark Fe_2Zr and light α-Fe nanolayers with relatively long straight layer interfaces. The inserted selected area diffraction (SAD) pattern shows diffraction from both α-Fe and Fe_2Zr with predominantly C15 structure, which is commonly accepted as the room temperature equilibrium phase. Fig. 2c shows the STEM image of the nanolaminates, wherein Fe_2Zr appears brighter due to its higher average atomic number than Fe. Fig. 2d shows a typical compositional line profile acquired across alternating layers over a distance of ~ 400 nm as shown in Fig. 2c. The composition profile of nanolaminate shows Fe and FeZr alloy with ~ 35 at.% Zr and 65 at.% Fe, corresponding to the Fe_2Zr intermetallic phase. $Fe_{23}Zr_6$ phase was also identified but scarce in the as-cast specimen.

For comparison, TEM micrographs of $Fe_{94.2}Zr_{5.8}$ alloy suction cast by using the cylinder mold are presented in Fig. 3. Similarly this specimen consists of α-Fe grains, straight laminar and cellular domains as shown in Fig. 3a. Fig. 3b shows a typical example of abundant straight nanolaminate patches separated by a grain boundary indicated by the dash line. The Fe_2Zr layers appear to contain planar defects parallel to layer interfaces. The SAD pattern of the nanolaminates in Fig. 3b is shown in Fig. 3c. Three phases were identified: α-Fe with zone axis of [011], and $Fe_{23}Zr_6$ and Fe_2Zr with respective zone axis of [011] and $[\bar{1}12]$. Hence, both specimens cast by the cylindrical and plate mold contain a small amount of $Fe_{23}Zr_6$ phase. High-density stacking faults in the Fe_2Zr phase are confirmed from the streaking lines in the SAD pattern. Although a majority of α-Fe grains were separated from nanolaminates by Fe_2Zr intermetallic layers, some locations were not separated as shown in Fig. 3d indicated by arrows. The direct contact of α-Fe grains with α-Fe in nanolaminates has implications on the thermal stability of nanocomposites as will be shown later from *in situ* annealing studies.

Annealing at various temperatures (for 1h) was performed to examine thermal stability of the as-cast FeZr nanocomposites. The indentation hardness (H_{IT}) of annealed alloys tested at room temperature is shown in Fig. 4. The hardness of alloys cast in different molds remains stable up to 700^{o}C, although the alloy fabricated in the cylinder mold has moderately higher hardness than that prepared by using the plate mold. After annealing at 900^{o}C, hardness of both alloys reduced moderately to ~ 3.5 GPa. In comparison, hardness of ultrafine grained (UFG) Fe

processed by equal channel angular pressing (ECAP) [28] decreased significantly above 250°C, to less than 1 GPa due to substantial grain coarsening.

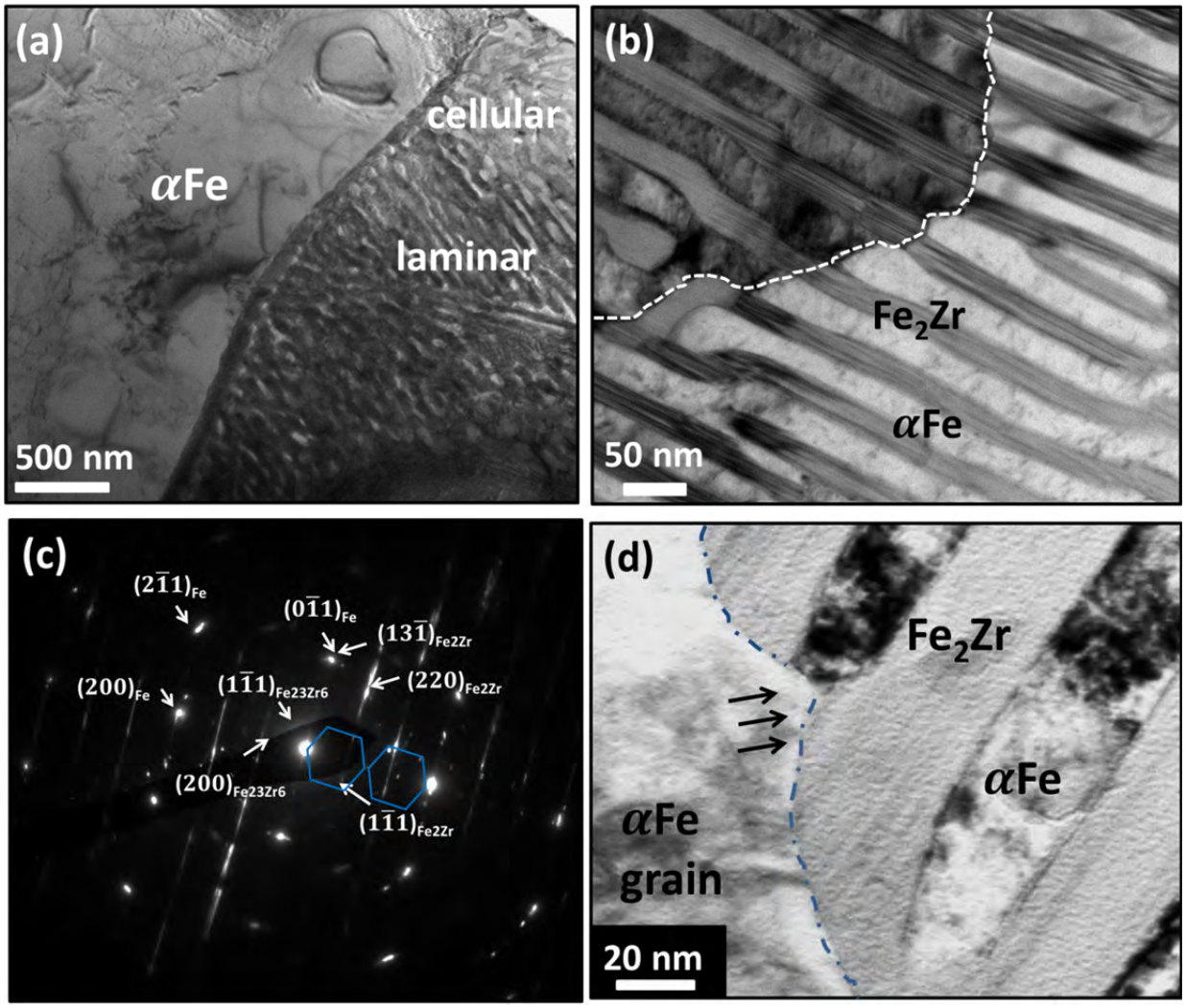

Figure 3. TEM images of different phases in $Fe_{94.2}Zr_{5.8}$ alloy prepared by suction casting using a cylinder mold. (a) Overview TEM images show the microstructure of as-cast alloy containing three phases: α-Fe grains, straight laminates and cellular phases. (b) TEM image shows the straight nanolaminates. The dashed line distinguishes the grain boundary between two different domains in the laminar region. (c) SAD pattern shows the existence of α-Fe, Fe_2Zr and $Fe_{23}Zr_6$, as well as stacking faults as indicated by streaking lines. Zone axis for α-Fe and $Fe_{23}Zr_6$ is <011>, and Fe_2Zr is <112>. (d) Higher magnification TEM image shows α-Fe grains and laminar phases are sometimes interconnected.

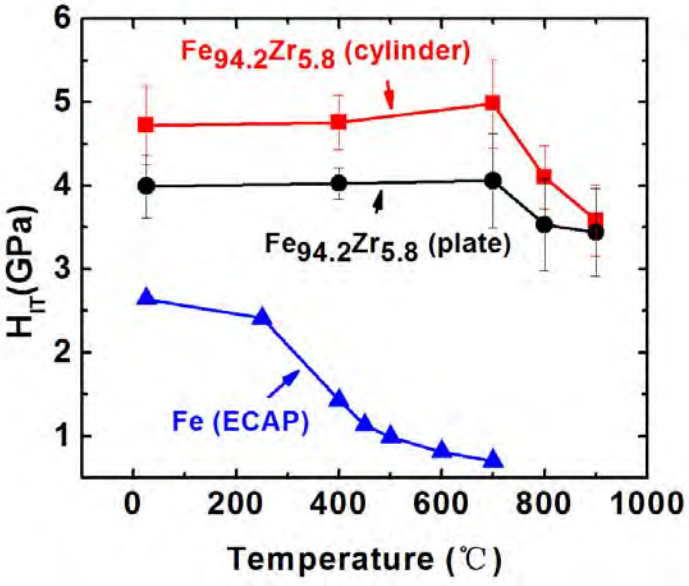

Figure 4. Hardness evolution of the FeZr nanocomposite with different Zr concentration after annealing at different temperatures. For comparison, data of pure Fe (solid triangle) [10] fabricated by equal channel angular pressing (ECAP) are also provided. Hardness of ECAPed Fe reduced rapidly at an annealing temperature of 250°C or greater, whereas the hardness of FeZr alloys decreased moderately at 800°C or higher.

Next we compare the microstructure of nanolaminates prepared by the cylinder and plate mold before annealing. The layer thicknesses of α-Fe and Fe_2Zr layers are nearly the same in both as-cast alloys. Nanocomposite prepared in the cylinder mold has a smaller average layer thickness, ~35 nm, compared with that cast by the plate mold, ~75 nm (Fig. 5).

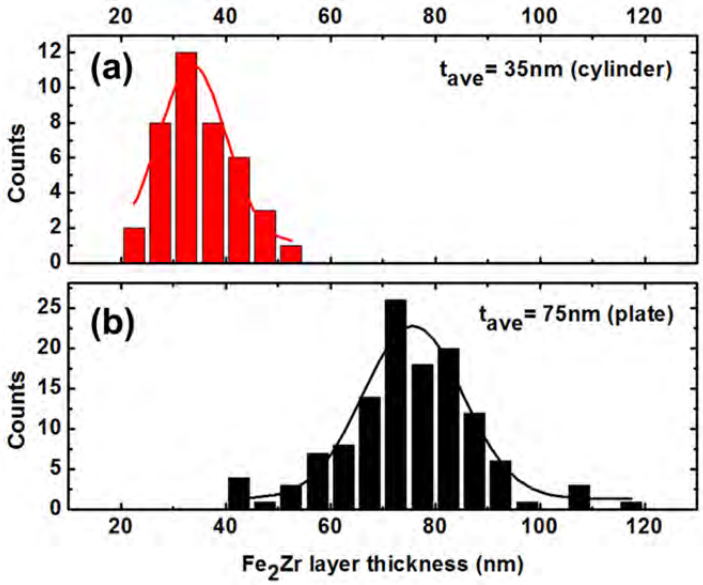

Figure 5. Comparison of laminar thickness of as cast $Fe_{94.2}Zr_{5.8}$ alloy prepared by using (a) cylinder mold and (b) plate mold. The average Fe_2Zr layer thickness is ~ 35nm for specimen cast in a cylinder mold, comparing to 75nm for that cast by a plate mold.

SEM images of the FeZr alloy (plate mold) annealed up to 900°C (800°C/1h and 900°C/0.5h) in Fig. 6 show the retention of all three componenents: α-Fe grains, nanolaminates and cellular patches.

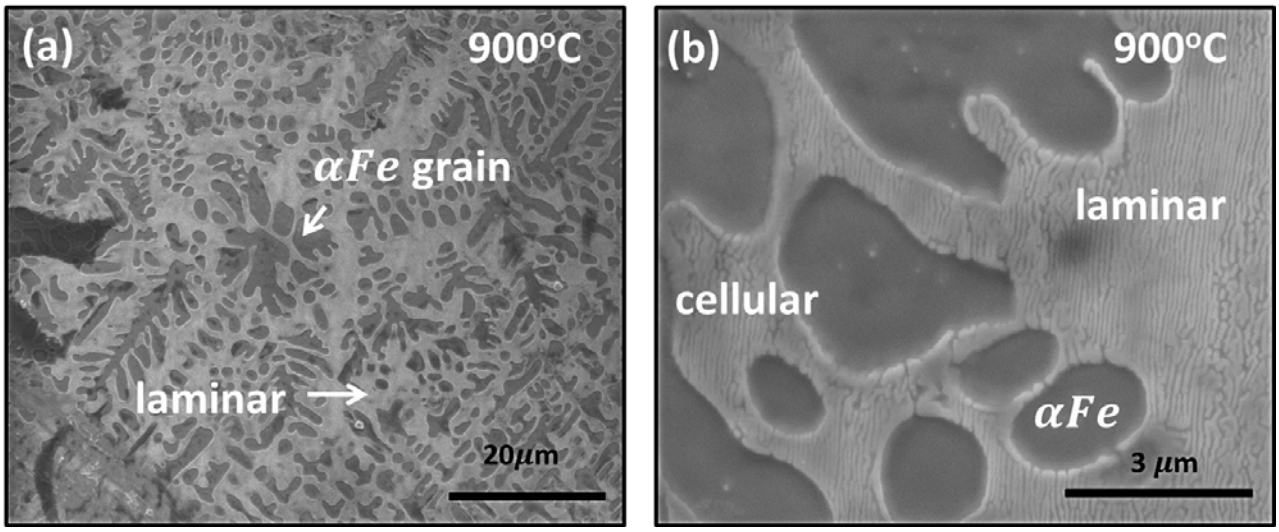

Figure 6. SEM images of $Fe_{94.2}Zr_{5.8}$ (plate mold) after *in situ* heating via 800°C/1h and then 900°C/0.5h. (a) Low magnification SEM image of the annealed $Fe_{94.2}Zr_{5.8}$ alloy showing the retention of laminar phases and relatively large grains. (b) High magnification SEM micrograph of the alloy with large grains and nanolaminates.

Statistical analysis shows that there is indeed some coarsening of microstructure in high-temperature annealed specimens. Fig. 7 shows that after annealing (800°C/1 h) the average grain size of α-Fe in $Fe_{94.2}Zr_{5.8}$ (plate mold), increased from 3.3 (as-cast) to 3.5 μm. Meanwhile the volume fraction of α-Fe grains increased from 43% to 47%, accompanied by the diminished volume fraction of nanolaminates and cellular components.

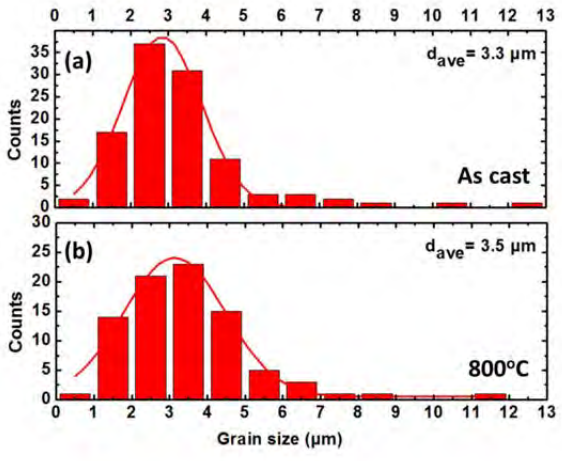

Figure 7. Grain size distribution of α-Fe grains in $Fe_{94.2}Zr_{5.8}$ (plate mold) before and after annealing (800°C/1h) obtained from SEM images. The average grain size of α-Fe grains enlarged from 3.3 to 3.5 μm. Meanwhile the volume fraction of α-Fe grains escalated from 43 to 47%.

In order to examine the microstructure evolution in more detail, *in situ* heating experiment were performed at a constant heating rate inside a transmission electron microscope. Snapshots captured during *in situ* heating (up to 650^{o}C) are shown in Fig. 8a-i. Several distinct events were captured in a typical region containing a large α-Fe grain encompassed by nanolaminates/cellular patches.

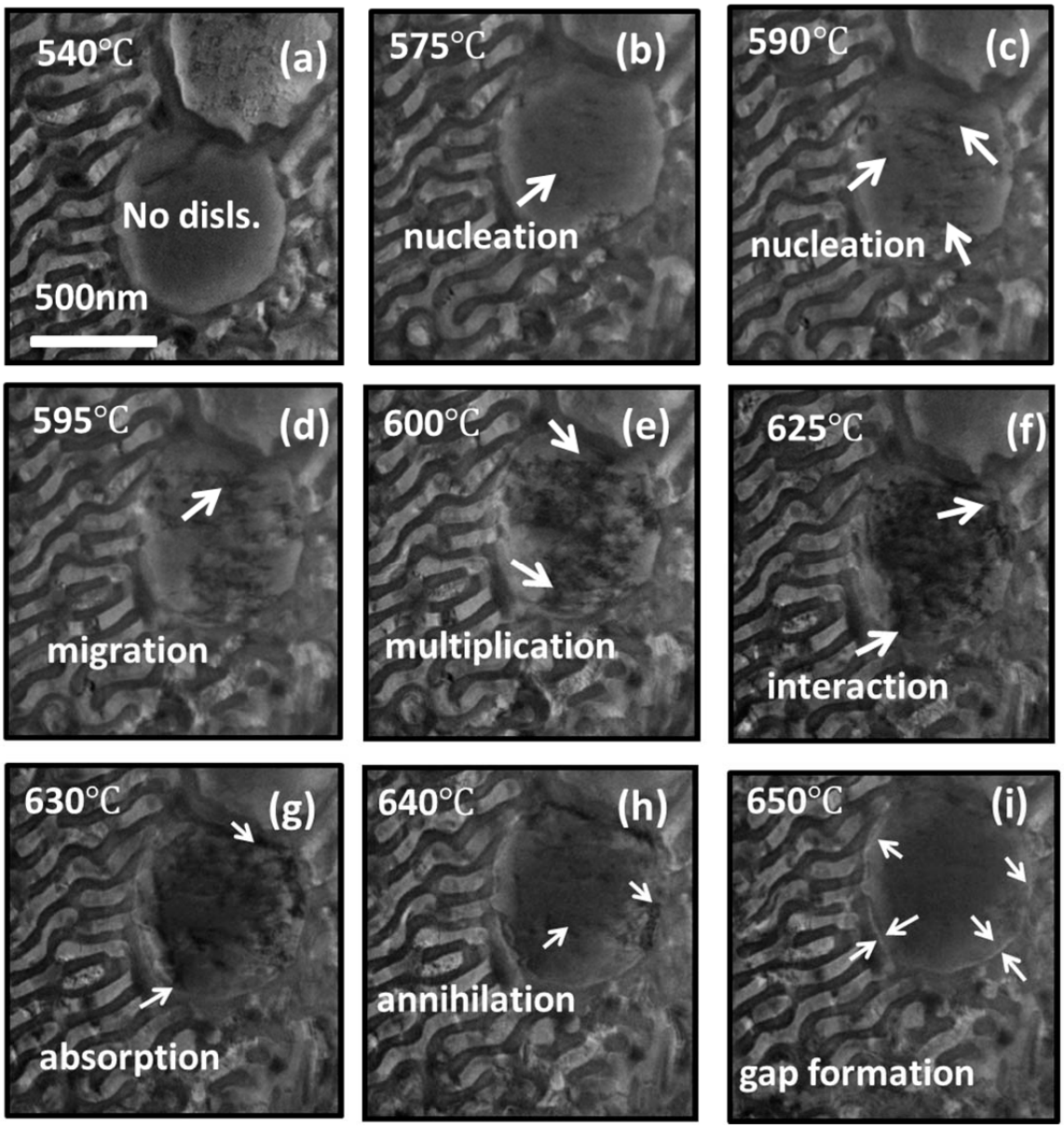

Figure 8. *In situ* TEM studies showing the evolution of dislocation density in α-Fe grain and the consequent formation of gap along its peripheral observed during *in situ* heating. (a) At 540^{o}C, almost no dislocations were observed in the α-Fe grain. (b) At 575^{o}C, several dislocations were nucleated inside the grain. (c) By 590^{o}C, more dislocations were nucleated in the grain. (d) At 595^{o}C, dislocation density increased across the whole grain.

(e) At 600^{o}C, dislocations proliferated and propagated rapidly toward the grain boundary. (f) At 625^{o}C, dislocation density reached the maximum level and dislocations interacted prominently with grain boundary. (g) Dislocations were annihilated at grain boundaries. Meanwhile the density of dislocations in grain interior started to decrease. (h) The density of dislocations in grain interior decreased significantly while dislocations continued their interactions with the grain boundary. (i) The substantial absorption of dislocations by the grain boundary led to creation of a gap surrounding the grain boundary.

First, no significant microstructure evolution was observed up to 540^{o}C (Fig. 8a). By 575^{o}C (Fig. 8b), several dislocations appeared in the α-Fe grain, manifesting a dislocation nucleation process. From 590^{o}C (Fig. 8c) to 595^{o}C (Fig. 8d), numerous additional dislocations emerged in the α-Fe grain, and some of these dislocations started to migrate. By 600^{o}C (Fig. 8e), the density of dislocations in the grain interior increased substantially. Meanwhile many of these dislocations appeared to propagate outwards and approached the boundary between the α-Fe grain and its nanolaminate peripherals, where interaction occurred (at ~ 625^{o}C in Fig. 8f). The dislocations arriving at the boundaries then interacted with phase boundaries and were annihilated (Fig. 8g and Fig. 8h). The continuous absorption of dislocations by domain boundaries led to the formation of a narrow gap, ~ ?? nm in width, surrounding the large α-Fe grain at 640^{o}C or higher temperature (Fig. 8i).

The microstructure evolution of nanolaminates was also investigated by *in situ* annealing. In general the nanolayer morphology remained thermally stable throughout the *in situ* heating study. In particular we observed an intriguing event involving migration of defect clusters in the α-Fe layer. Figure 9a-f show that a defect cluster (outlined in red dash circle) in the α-Fe layer adjacent to the boundary between α-Fe grain and nanolaminate propagated leftward. The migration of the defect cluster appeared confined in the α-Fe layer, and no sign of interaction between the defect cluster and the laminar interface was observed.

A comparison of microstructural stability of various components in FeZr nanocomposites is shown in Fig. 10 after *in situ* annealing up to 800^{o}C/1 h. As shown in Fig. 10a, several defect clusters appeared in the α-Fe layer in the cellular domains and some gaps were observed surrounding large α-Fe grains. In contrast, Fig. 10b shows that the nanolaminates retained the straight laminar interface after annealing under the same condition.

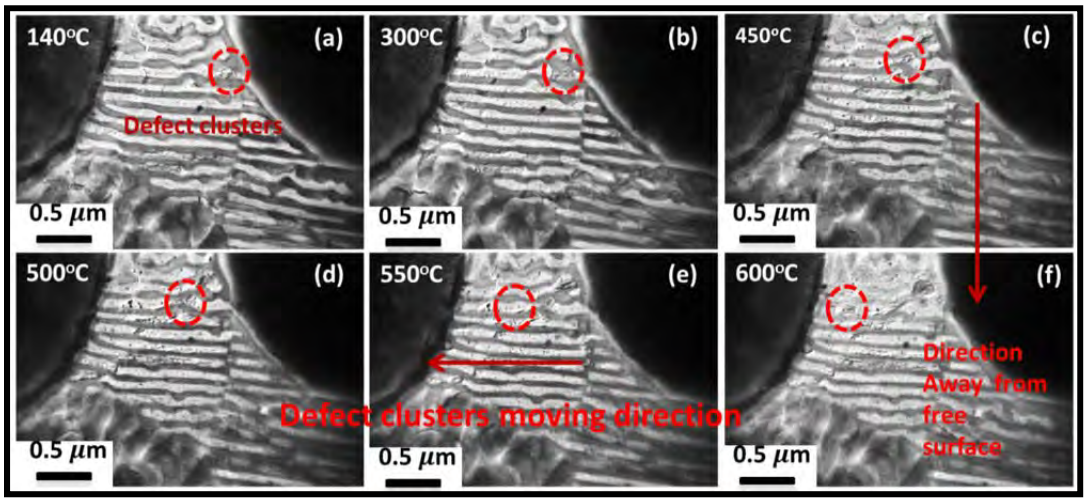

Figure 9. Defect cluster migration in the nanolaminate captured during *in situ* heating study. (a) Defect clusters reside in the α-Fe layer adjacent to the boundary between nanolaminate and the α-Fe grain. (b-e) A defect cluster (highlighted in a red dashed circle) first propagated leftwards away from the boundary. Then the defect cluster migrated within the α-Fe layer and changed its geometry continuously. (f) The defect cluster stopped propagating and remained in the α-Fe layer.

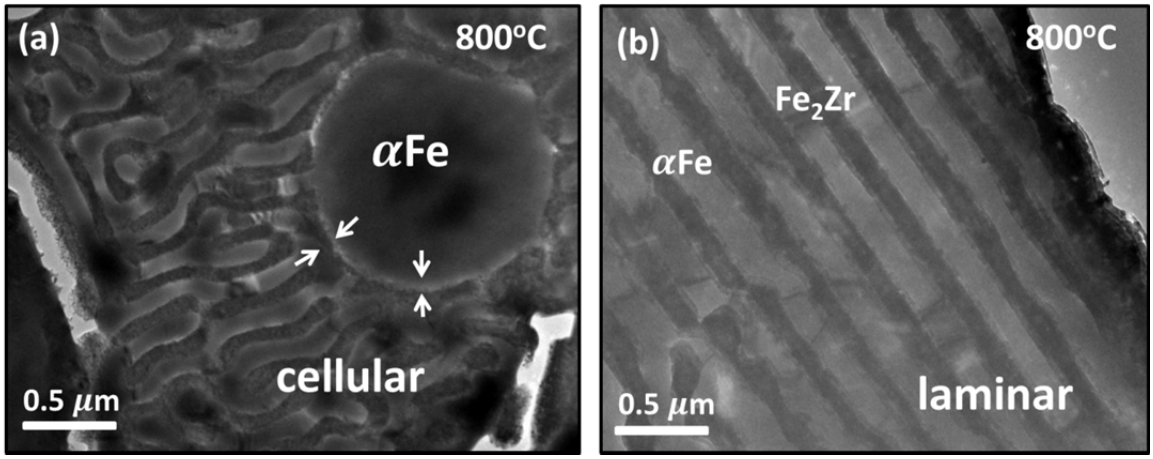

Figure 10. TEM micrograph of $Fe_{94.2}Zr_{5.8}$ alloy cast by plate mold after *in situ* annealing at 800°C for 1h. (a) In area containing large α-Fe grains and cellular domains, some defect clusters are observed in α-Fe layer of the cellular domains, and a gap appeared surrounding the annealed large α-Fe grains. (b) Area composed of long straight laminates remained very stable after high temperature annealing.

3.1.4. Discussion

Hardness evolution due to coarsening of microstructures

As-cast FeZr nanocomposites contain several major components: straight nanolaminates, cellular domains and large α-Fe grains. Nanolaminates, consisting of alternating Fe_2Zr and α-Fe layers, which is the product of eutectic phase transformations, have outstanding thermal stability and mechanical strength. Meanwhile α-Fe grains may sustain considerable ductility in the nanocomposite. Hence the interesting combination of these two structural motifs may render high strength and ductility in nanocomposites [38].

The hardness of the nanocomposites with multiple components may be estimated from a simple rule-of-mixture method as follows:

$$H_{composite} = H_{eutectic} * f_{eutectic} + H_{Fe} * f_{Fe} \quad (1),$$

where $H_{composite}$, $H_{eutectic}$, and H_{Fe} represent the hardness of composite, eutectic phase and α-Fe grain, respectively. $f_{eutectic}$ and f_{Fe} are the respective volume fraction of the eutectic phase (including nanolaminates and cellular domains) and α-Fe grains.

The weight percentage of α-Fe phase ($W_{Fe}\%$) in the composites estimated by lever rule is 40%. Considering that density of pure Fe and Fe_2Zr phase [41] is similar, the volume fraction of α-Fe grains should be also ~ 40%, which agrees well with 43%, measured experimentally from SEM analysis.

The hardness of as-cast FeZr cylindrical specimen is greater than that cast by plate mold. The volume fraction and average grain size of α-Fe grains in both specimens are very close to each other. However the average laminar thickness for the cylindrical specimen is ~ 35 nm, much smaller than that cast by plate mold, ~75nm. Such difference in layer thickness arises from the difference in cooling rate during rapid solidification process. The cylindrical specimen has smaller volume and greater surface thus solidification time is ~ 40% shorter that achieved in the plate mold according to Chvorinov's rule [42] (assuming the mold constant is identical for both molds). A higher quenching rate leads to smaller average laminar thickness, which in turn induces greater hardness in metallic nanolaminates [43-47]. Consequently the hardness of the cylindrical specimen is greater than that of the plate specimen.

Prior studies show that the hardness of ECAPed UFG Fe quickly decreases beyond 250^{o}C

due primarily to grain growth, and by 400^{o}C, its hardness drops significantly to 1 GPa. The addition of Zr to pure Fe by ball-milling can significantly enhance the thermal stability of nanocrystalline Fe grains [13], but softening occurred in this alloy at an annealing temperature of ~ 550^{o}C. Our study shows that the $Fe_{94.2}Zr_{5.8}$ nanocomposites retain their hardness up to 700^{o}C, and remain as strong as ~3.5 GPa upon further annealing to 900^{o}C. Decreasing the concentration of Zr (to 4 at. %) in the nanocomposite (not reported here) follows the same trend.

In spite of their extraordinary thermal stability, the FeZr nanocomposites in both systems soften gradually after annealing above 700^{o}C. Microscopy studies show that the average laminar thickness of the as-cast and annealed samples (800^{o}C/1h) is nearly the same, but the average grain size of α-Fe grains increases from 3.3 to 3.5 μm (Fig. 7), corresponding to an almost 10% increase in volume fraction of large grains. As shown in equ. (1), the coarsening and increase in volume fraction of soft α-Fe grains ($f_{\alpha Fe}$) and the correlated decrease in the volume fraction of the strong eutectic nanolaminate ($f_{eutectic}$) should account for the softening after annealing.

Other factors that may contribute to softening could involve the chemistry and instability of cellular domains. In contrast to the long and straight interfaces in nanolaminates, cellular domains have discontinuous and curved layer interfaces, and are more prone to coarsening. Meanwhile it is also interesting to note that $Fe_{23}Zr_6$ is more frequently found in the cellular domains than in straight nanolaminates. Comparing with Fe_2Zr, the metastable $Fe_{23}Zr_6$ phase, enriched in Fe, could become less stable upon high temperature annealing, and may transport excess Fe atoms to large α-Fe grains.

It has been reported that lamellar structure in eutectic alloys can coarsen because of direct cylinderization, edge spheroidization, boundary splitting, and termination migration etc.. However these phenomena are not observed in annealed Fe/Fe_2Zr nanolaminate, which is stable after annealing at 800^{o}C/1h. We speculate that FeZr nanocomposite with predominantly long straight nanolaminates and less cellular domains could have enhanced thermal stability comparing with the current system.

Thermal stress induced plastic yielding of large α-Fe grains due to nucleation of dislocations

In situ heating studies (Fig. 8) show several distinctive events in α-Fe grains, including

nucleation of dislocations, propagation of dislocations toward grain boundaries, annihilation of dislocations by boundaries followed by the generation of a ring of gap surrounding α-Fe grains.

The nucleation of dislocations will be examined first. It is well known that under external stress, dislocations can nucleate in metallic materials, signaling the plastic yielding of grains. During *in situ* heating study, however, there is no external applied stress. Hence it is necessary to evaluate the sources of stress that lead to the observed nucleation of dislocations in α-Fe grains. We hypothesize that one of such sources could be thermal stress.

TEM studies show that large α-Fe grains are typically surrounded by a thin layer of Fe_2Zr (Fig. 2, Fig. 3). As the thermal expansion coefficient (TEC) of Fe and Fe_2Zr is different, thermal stress arises during *in situ* annealing. If the magnitude of the thermal stress exceeds the yield strength of α-Fe grains, then dislocations may nucleate. In order to validate such a hypothesis, we first estimate the magnitude of thermal stress (σ_t) by using

$$\sigma_t = E\varepsilon_t = E(\alpha_{Fe} - \alpha_{Fe_2Zr}) * \Delta T \quad (2),$$

where ε_t is the thermal mismatch strain, E is the Young's modulus of Fe, α_{Fe} and α_{Fe_2Zr} are the respective TEC of the α-Fe and Fe_2Zr phase, and ΔT is the change in temperature.

The TEC of Fe varies slightly: $10.4 \times 10^{-6}\,K^{-1}$ for cast Fe, $11.8\times10^{-6}\,K^{-1}$ for pure Fe, and $11\times10^{-6}\,K^{-1}$for forged Fe. According to [48], TEC of Fe at high temperature range is even larger than at room temperature. The TEC value of Fe_2Zr phase in $Fe_{67}Zr_{33}$, $Fe_{70}Zr_{30}$, and $Fe_{72}Zr_{28}$ can be estimated as 2.91, 3.91, and $4.73\times10^{-6}\,K^{-1}$ [41]. In this study, we selected TEC of Fe as $10.4 \times 10^{-6}\,K^{-1}$ and Fe_2Zr as $4.73\times10^{-6}\,K^{-1}$, which may lead to slightly underestimation of thermal stress. At 575°C (Fig. 8) when dislocations begin to nucleate as evidenced from *in situ* studies, the thermal stress is estimated to be ~ 670 MPa.

Next, we need to estimate the yield strength of large α-Fe grains via Hall-Patch relation:

$$\sigma = \sigma_0 + k_y d^{-0.5} \quad (3),$$

where σ_0 is friction stress, ~ 25MPa for Fe, and k_y is the locking parameter, ~ 0.6 $MPa\bullet m^{-1/2}$ for Fe [49, 50]. Thus the yield strength for the α-Fe grain (in the *in situ* video) with a grain size of 1.4 μm (as shown in Fig. 8) is ~530 MPa. Clearly the TEC mismatch induced stress exceeds the yield strength, and hence dislocations can nucleate at 575°C, in good agreement with

the *in situ* experimental observation.

The generation of gaps and coarsening of α-Fe grains

The observation of gaps surrounding the α-Fe grain induced during annealing is an intriguing phenomenon. As revealed by *in situ* heating studies, the nucleated dislocations traveled toward grain boundaries where they were annihilated afterwards. Continuous absorption of dislocations by grain boundaries eventually lead to large plastic deformation along grain boundaries (which is also phase boundary between α-Fe and Fe_2Zr). The continuous absorption of dislocations may weaken the bonding between α-Fe and Fe_2Zr and their phase boundaries and lead to delamination, manifested by the formation of a ring of gaps. The creation of gaps may encourage the diffusion of Fe atoms from α-Fe layer in the nanolaminate to the α-Fe grains, leading to grain coarsening as observed in this study. The discontinuous phase boundaries between nanolaminates and large grains (Fig. 3d) may also become channels that permit the diffusion of Fe atoms from cellular/laminar phase to α-Fe grains.

On the other hand, the large thermal stress induced by TEC cannot lead to interfacial delamination between α-Fe and Fe_2Zr layers in nanolaminates. The α-Fe layer in nanolaminate has much greater yield strength than its coarse grained counterpart. At the current length scale, ~ 35-70 nm, the yield strength of α-Fe layers in the laminate could exceed 1 GPa. Hence fewer dislocations can be generated in the α-Fe layer in the nanolaminate. Correspondingly we observed sporadic migration of defect clusters confined within the α-Fe layers in nanolaminates (Fig. 9). It is interesting to note that the mobile defect clusters in the α-Fe nanolayer are often initiated from the α-Fe grain boundaries, where α-Fe nanolayer is in direct contact to the α-Fe grains. The nucleation of dislocations (from 575^{o}C) and the subsequent gap formation (at 650^{o}C) observed from the *in situ* videos matches well with the *ex situ* hardness measurements which show that the softening of FeZr nanocomposites gradually starts from 700^{o}C (Fig. 4).

A schematic illustrating the microstructural evolution of the FeZr nanocomposite is shown in Fig. 11. The FeZr nanocomposite contains α-Fe grains embedded in the nanolaminate and cellular matrix (Fig. 11a), and a nearly continuous Fe_2Zr phase boundary separates the α-Fe grains from laminar/cellular components. Beyond a critical temperature T_1 (Fig. 11b), dislocations are nucleated as TEC mismatch induced stress exceeds the yield strength of α-Fe

grains. At even greater temperature T_2 (Fig. 11c), dislocations reach and interact with the phase boundary, forming a ring of gaps. The gap can be backfilled by the diffusion of Fe atoms (at T_3) from cellular/laminar domains, corresponding to the gradual growth of α-Fe grains. Sporadic defect clusters may also be present in the α-Fe layer in nanolaminates. But their density is in general low, and insufficient to lead to debonding of layer interface. Nanolaminates are very stable throughout the entire annealing studies.

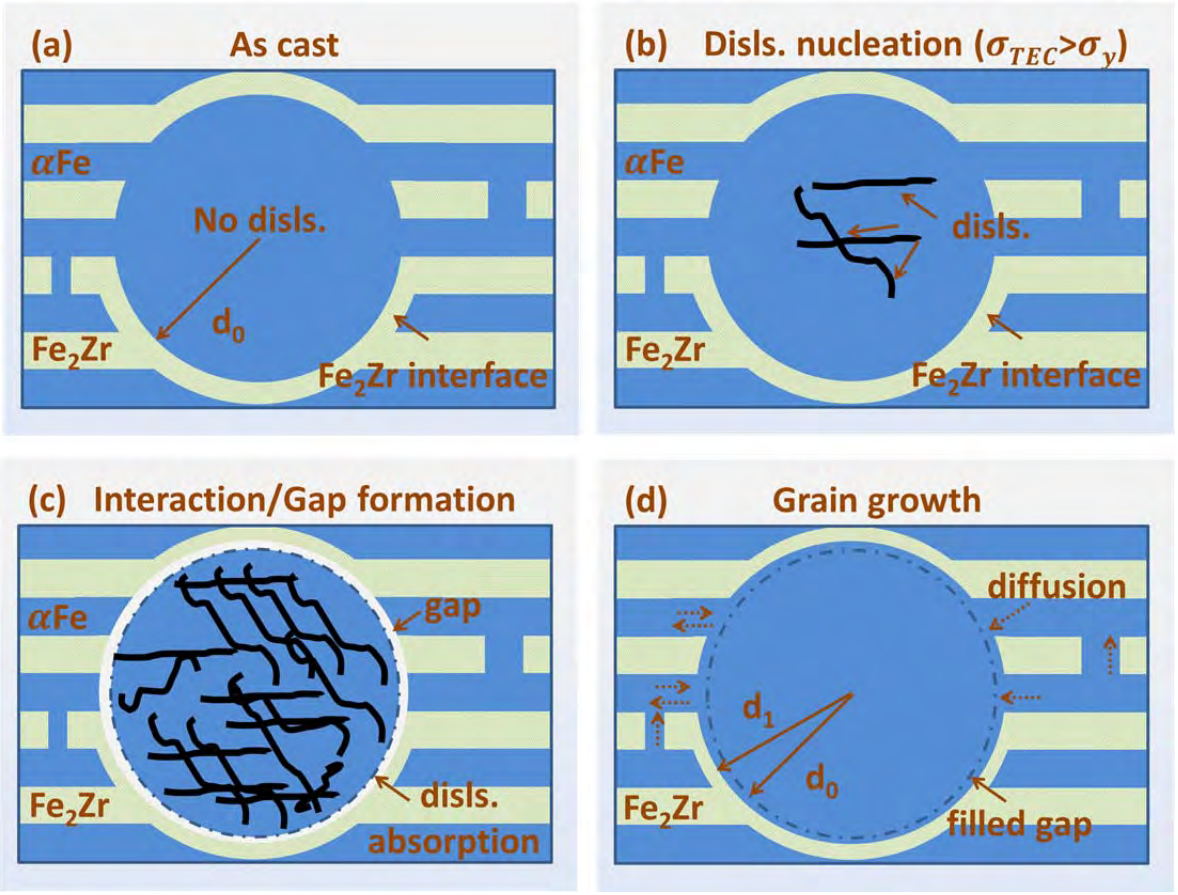

Figure 11. Schematic of a grain growth mechanism for α-Fe grain under high temperature annealing. (a) As cast nanocomposite contains α-Fe grains separated by patches of nanolaminates. (b) At elevated temperature, dislocations start to nucleate in α-Fe grain interior when thermal expansion mismatch (between α-Fe grain and the Fe_2Zr at phase boundary) induced stress exceeds the yield strength of the α-Fe grain. Meanwhile, some defect clusters are nucleated in the α-Fe nanolaminates. (c) Dislocation density in the α-Fe grain increases sharply and dislocations propagate towards and interact with phase boundary. The phase boundary continuously absorbs these dislocations until it cannot accommodate ever increasing dislocations, then a gap is created along the phase boundary. (d) The diffusion of Fe atoms from the α-Fe nanolaminates to the α-Fe grains fill in the gap, and leads to subsequent grain growth and gradual removal of nanolaminates.

Conclusions

FeZr nanocomposites containing nanolaminate matrix exhibit extraordinary thermal stability up to ~ 900^{o}C. Softening beyond 700^{o}C results from coarsening of large α-Fe grains. *In situ* study shows that mismatch in thermal expansion coefficient between Fe and Fe_2Zr induced significant thermal stress that could exceed the yield strength of α-Fe grains, manifested by nucleation and migration of dislocations towards phase boundaries. The absorption of dislocations leads to debonding along phase boundaries manifested by the formation of a narrow gap, which permits the diffusion of Fe from nanolaminates to large α-Fe grains, leading to their coarsening. In contrast, nanolaminates away from α-Fe grains are very stable up to 900^{o}C.

References

[1] Y. H. Zhao, H. W. Sheng, K. Lu, "Microstructure evolution and thermal properties in nanocrystalline Fe during mechanical attrition", Acta Mater., 49, 365-375, (2001).
[2] C. H. Moelle, H. J. Fecht, "Thermal stability of nanocrystalline iron prepared by mechanical attrition", Nanostruct. Mater., 6, 421-424, (1995).
[3] T. R. Malow, C. C. Koch, "Grain growth in nanocrystalline iron prepared by mechanical attrition", Acta Mater. 45, 2177-2186, (1997).
[4] H. Natter, M. Schmelzer, R. Hempelmann, "Nanocrystalline nickel and nickel-copper alloys: synthesis, characterization, and thermal stability", J. Mater. Res., 13(5), (1998).
[5] U. Klement, U. Erb, A. M. El-Sherik, K. T. Aust, "Thermal stability of nanocrystalline Ni", Scripta Mater., 203, 177-186, (1995).
[6] R. Klemm, E. Thiele, C. Holste, J. Eckert, N. Schell, "Thermal stability of grain structure and defects in submircocrystalline and nanocrystalline nickel", Scripta Mater., 46, 685-690, (2002).
[7] M. Thuvander, M. Abraham, A. Cerezo, G. D. W. Smith, "Thermal stability of electrodeposited nanocrystalline nickel and iron-nickel alloys", Mater. Sci. Technol., 17, 961, (2001).
[8] L. Lu, L. B. Wang, B. Z. Ding, K. Lu, "Comparison of the thermal stability between electro-deposited and cold-rolled nanocrystalline copper samples", Mater. Sci. Eng., A, 286, 125-129, (2000).
[9] L. Lu, N. R. Tao, L. B. Wang, B. Z. Ding, K. Lu, "Grain growth and strain release in nanocrystalline copper", J. Appl. Phys., 89, 6408 (2001).
[10] L. H. Qian, S. C. Wang, Y. H. Zhao, K. Lu, "Microstrain effect on thermal properties of nanocrystalline Cu", Acta Mater., 50, 3425-3434, (2002).
[11] H. Jiang, Y. T. Zhu, D. P. Butt, I. V. Alexandrov, T. C. Lowe, "Microstructural evolution, microhardness and thermal stability of HPT-processed Cu", Mater. Sci. Eng., A, 290, 128-138, (2000).
[12] L. Lu, N. R. Tao, L. B. Wang, B. Z. Ding, K. Lu, "Grain growth and strain release in nanocrystalline copper", J. Appl. Phys., 89, 6408, (2001).
[13] K. A. Darling, B. K. Vanleeuwen, C. C. Koch, R. O. Scattergood, "Thermal stability of nanocrystalline Fe-Zr alloys", Mater. Sci. Eng., A, 527, 3572-3580, (2010).

[14] K. A. Darling, R. N. Chan, P. Z. Wong, J. E. Semones, R. O. Scattergood, C. C. Koch, “Grain-size stabilization in nanocrystalline FeZr alloys, Scripta. Mater. 59, 530-533, (2008).
[15] T. Chookajorn, H. A. Murdoch, C. A. Schuh, “Design of stable nanocrystalline alloys”, Science, 337, 951, (2012).
[16] Y. Chen, Y. Liu, F. Khatkhatay, C. Sun, H. Wang, X. Zhang, “Significant enhancement in the thermal stability of nanocrystalline metals via immiscible tri-phases”, Scripta. Mater., 67, 177-180, (2012).
[17] X. Zhang, A. Misra, “Superior thermal stability of coherent twin boundaries in nanotwinned metals”, Scripta. Mater., 66, 860-865, (2012).
[18] O. Anderoglu, A. Misra, H. Wang, X. Zhang, “Thermal stability of sputtered Cu films with nanoscale growth twins”, J. Appl. Phys., 103, 094322, (2008).
[19] D. Bufford, H. Wang, X. Zhang, “Thermal stability of twins and strengthening mechanisms differently oriented epitaxial nanotwinned Ag films”, J. Mater. Res., 28, 1729, (2013).
[20] X. Zhang, A. Misra, H. Wang, T. D. Shen, M. Nastasi, T. E. Mitchell, J. P. Hirth, R. G. Hoagland, J. D. Embury, “Enhanced hardening in Cu/330 stainless steel multilayers by nanoscale twinning”, Acta Mater. 52, 995-1002, (2004).
[21] X. Zhang, R. K. Schulze, H. Wang, A. Misra, “Thermal stability of sputtered Cu/304 stainless steel multilayer films”, J. Appl. Phys., 101, 124311, (2007).
[22] A. Misra, R. G. Hoagland, H. Kung, “Thermal stability of self-supported nanolayered Cu/Nb films”, Philos. Mag., 84, 1021-1028, (2004).
[23] D. H. Ryan, J. M. D. Coey, “Magnetic properties of iron-rich Fe-Zr glasses”, Phys. Rev. B, 35, 8630, (1987).
[24] L. F. Kiss, G. Huhn, T. Kemeny, J. Balogh, D. Kaptas, “Magnetic properties of Fe-Zr metastable phases”, J. Magn. Magn. Mater., 160, 229-232, (1996).
[25] H. Hiroyoshi, K. Fukamichi, “Ferromagneticspin glass transition in FeZr amorphous alloy system”, J. Appl. Phys. 53, 2226, (1982).
[26] K. Fukamichi, R. J. Gambino, T. R. McGuire, “Electrical resistivity and Hall effect in FeZr amorphous sputtered films”, J. Appl. Phys. 53, 2310, (1982).
[27] E. Hellstern, L. Schultz, “Progress of the amorphization reaction during mechanical alloying in FeZr”, J. Appl. Phys. 63, 1408, (1988).
[28] K.A. Darling, B.K. Vanleeuwen, C.C. Koch, R.O. Scattergood, “Thermal stability of nanocrystalline Fe-Zr alloys”, Mater. Sci. Eng., A, 527, 3572-3580, (2010).
[29] Y. Liu, J.D. Livingston, S.M. Allen, “Room-temperature deformation and stress-induced phase transformation of laves phases in Fe-10 at. Pct Zr alloy”, Metall. Trans. A, 23A, 3303-3308, (1992).
[30] D. P. Abraham, J. W. Richardson Jr. S. M. McDeavitt, “Laves intermetallics in stainless steel-zirconium alloys”, Mater. Sci. Eng., A, 239-240, 658-664, (1997).
[31] K. Y. Yu, Z. Fan, Y. Chen, M. Song, Y. Liu, H. Wang, M. A. Kirk, M. Li, X. Zhang, “In situ observation of defect annihilation in Kr ion-irradiated bulk Fe/amorphous-Fe_2Zr nanocomposite alloy”, …(2014).
[32] S. M. McDeavitt, D. P. Abraham, J. Y. Park, “Evaluation of stainless steel-zirconium alloys as high-level nuclear waste forms”, J. Nucl. Mater., 257, 21-34, (1998).
[33] S. Chatain, C. Gueneau, C. Chatillon, “High temperature mass spectrometry: application to the thermodynamic study of Fe-Zr system”, J. Nucl. Mater., 344, 281-284, (2005).
[34] C. Wei, A. Aitkaliyeva, Z. Luo, A. Ewh, Y.H. Sohn, J.R. Kennedy, B.H. Sencer, M.T. Myers, M. Martin, J. Wallace, M.J. General, L. Shao, “Understanding the phase equilibrium and

irradiation effects in Fe-Zr diffusion couples”, J. Nucl. Mater., 432, 205-211, (2013).
[35] D.P. Abraham, J.W. Richardson Jr., “Phase stability of laves intermetallics in a stainless steel-zirconium alloy”, TMS Annual Meeting, San Diego, CA (US), (1999).
[36] F. Stein, G. Sauthoff, M. Palm, “Experimental determination of intermetallic phases, phase equilibria, and invariant reaction temperatures in the Fe-Zr system”, J. Phase Equilib., 23(6), (2002).
[37] H. Okamoto, “Fe-Zr (Iron-Zirconium)”, J. Phase Equilib. Diff., 27(5), (2006).
[38] J.M. Park, S.W. Sohn, T.E. Kim, D.H. Kim, K.B. Kim, W.T. Kim, “Nanostructure-dendrite composites in the FeZr binary alloys system exhibiting high strength and plasticity”, Scripta. Mater, 57, 1153-1156, (2007).
[39] E. G. Fu, A. Misra, H. Wang, L. Shao, X. Zhang, “Interface enabled defects reduction in helium ion irradiated Cu/V nanolayers”, J. Nucl. Mater., 407, 178-188, (2010).
[40] R. Saha, W. D. Nix, “Effects of the substrate on the determination of thin film mechanical properties by nanoindentation”, Acta Mater., 50, 23-28, (2002).
[41] N. Mattern, W.X. Zhang, S. Roth, H.Reuther, C. Baehtz, M. Richter, “Structural and magnetic properties of non-stoichiometric Fe_2Zr”, J. Phys.: Condens. Matter, 19, 376202(8pp), (2007).
[42] “Theory of the solidification of castings”, Giesserei, 27, 177-186, (1940).
[43] E. G. Fu, Nan Li, A. Misra, R. G. Hoagland, H. Wang, X. Zhang, “Mechanical properties of sputtered Cu/V and Al/Nb multilayers films”, Mater. Sci. Eng., A, 493, 283-287, (2008).
[44] Y. Liu, D. Bufford, H. Wang, C. Sun, X. Zhang, “Mechanical properties of highly textured Cu/Ni multilayers”, Acta Mater., 59, 1924-1933, (2011).
[45] N. Li, K. Y. Yu, J. Lee, H. Wang, X. Zhang, “Size dependent strengthening mechanisms in sputtered Fe/W multilayers”, J. Appl. Phys. 107, 093503, (2010).
[46] J. Y. Zhang, Y. Liu, J. Chen, Y. Chen, G. Liu, X. Zhang, J. Sun, “Mechanical properties of crystalline Cu/Zr and crystal-amorphous Cu/Cu-Zr multilayers”, Mater. Sci. Eng., A, 552, 392-298, (2012).
[47] X. Zhang, O. Anderoglu, R. G. Hoagland, A. Misra, “Nanoscale growth twins in sputtered metal films”, Twinning in nanometals, Overview.
[48] F. C. Nix, D. MacNair, “The thermal expansion of pure metals: copper, gold, aluminium, nickel, iron”, Phy. Rev., 60, (1941).
[49] Y. Bergstrom, H. Hallen, “Hall-Patech relationships of iron and steel”, Metal Science, 17, 341-347, (1983).
[50] J. S. C. Jang, C. C. Koch, “The hall-petch relationship in nanocrystalline iron produced by ball milling”, Scripta. Mater., 24, 1599-1604, (1990).

3.2. *In situ* Observation of Defect Annihilation in Kr Ion Irradiated Bulk Fe/Amorphous-Fe_2Zr Nanocomposite Alloy (K. Y. Yu, *et al*, Materials Research Letters, **DOI:**10.1080/21663831.2014.951494, 2014)

Abstract

Enhanced irradiation tolerance in crystalline multilayers has received significant attention lately. However, little is known on the irradiation response of crystal/amorphous nanolayers. We

report on *in situ* Kr ion irradiation studies of a bulk $Fe_{96}Zr_4$ nanocomposite alloy. Irradiation resulted in amorphization of Fe_2Zr and formed crystal/amorphous nanolayers. α-Fe layers exhibited drastically lower defect density and size than those in large α-Fe grains. *In situ* video revealed that mobile dislocation loops in α-Fe layers were confined by the crystal/amorphous interfaces and kept migrating to annihilate other defects. This study provides new insights on the design of irradiation tolerant crystal/amorphous nanocomposites.

Next generation nuclear energy technology requires advanced structural materials that must withstand extreme irradiation environments.[1-3] One of the emerging approaches is to introduce abundant interfaces by forming nanostructures in the materials. [4, 5] Consisting of two or more nanostructured heterophases, metallic nanolaminates exhibit not only excellent mechanical strength[6-9] and fatigue resistance,[10] but impressive tolerance to ion irradiation.[11-13] He ion irradiation studies have been extensively reported in immiscible nanolaminates such as Cu/V,[14-16] Cu/Nb[11], Cu/W,[17] Cu/Mo,[18] Ag/Ni[19] and Ag/V[20] and miscible Al/Nb[21] and Fe/W[22]. Defect density and irradiation induced hardening in these systems show a strong size dependence on individual layer thickness (*h*), that is the magnitude of irradiation hardening and defect density both decrease at smaller *h* in immiscible nanolaminates. Fu *et al.* first showed prominent simultaneous reduction of irradiation hardening and He bubble density in He ion irradiated Cu/V system when *h* is smaller[16]; similar phenomena were later observed in several other systems, such as Ag/Ni,[19] Ag/V[20] and Fe/W.[22] Molecular dynamics (MD) simulations[23] pointed out that layer interfaces can act as effective defect sinks for irradiation induced point defects.[24] Thus the size dependence is because that smaller *h* gives rise to greater interfacial area per unit volume, which provides more sinks to irradiation induced point defects and clusters.

The nature of such sinks is not quite well understood to date as there are only a handful of studies on irradiation damage in nanolaminates with different types of interfaces. In general these studies can be classified into systems with miscible and immiscible interfaces. Miscible interfaces are prone to irradiation induced mixing and hence may be less effective to sustain irradiation damage at higher dose and temperature.[21, 22] In immiscible systems, several types of interfaces have been investigated, such as fcc/bcc,[12, 14] bcc/bcc[22] and fcc/fcc[19, 25], where fcc and bcc stand for face-centered cubic and bcc-body centered cubic, respectively. The

efficiency of the immiscible interfaces to capture and annihilate point defects might be related to the density of misfit dislocations at the interfaces.[12] Yu *et al.* recently reported *in situ* evidence of fast migration of defect clusters towards Ag/Ni layer interfaces decorated with high density misfit dislocations. And the interactive energy needed to annihilate two loops with opposite nature was estimated to be ~0.4 eV.[25]

In situ irradiations performed while imaging with a transmission electron microscope provides important insights for investigating dynamics of defect-defect and defect-interface interactions thanks to real-time observation of microstructural evolution in irradiated materials. Numerous phenomena have been observed using *in situ* irradiation technique, such as anisotropic void formation in Mg,[26] irradiation induced grain growth in Fe and Zr,[27] defect absorption by triple junctions in nc Ni,[28] defect removal by twin boundaries (TBs) and the irradiation induced TB migrations in nanotwinned metals,[29, 30] and defect migration kinetics in nanoporous metals [31-33]. Meanwhile several *in situ* mechanical testing studies are also available [34, 35].

Most prior studies on multilayers focused on thin films (several μm in thickness), whereas the application in nuclear reactors typically calls for bulk nanocomposites. [2, 3, 5] Irradiation studies on bulk nanolaminate alloys remain scarce.[36] What is more, there is no investigations on irradiation response of nanocomposites with crystal/amorphous interfaces. In this study, we report on *in situ* studies on the heavy ion irradiation response of a bulk FeZr nanocomposites consisting of Fe/Fe_2Zr nanolaminates and submicron α-Fe grains prepared by suction casting technique. Low dose irradiation leads to amorphization of Fe_2Zr layers and subsequent formation of Fe/amorphous Fe_2Zr nanolaminates. The crystal/amorphous layer interface has extraordinary stability against irradiation and the confined migration of dislocation loops within α-Fe layers reduces their defect density significantly.

The Fe-4 at.% Zr alloy was prepared by melting high-purity iron (99.95%) and zirconium (99.8%) using an Edmund Buhler AM arc melting machine. The raw materials were remelted multiple times (for homogeneity) in water cooled Cu crucibles under an ultra high purity (UHP) argon (Ar) atmosphere and solidified rapidly by suction casting technique. The chamber was pumped down to a vacuum of 3×10^{-3} Pa prior to melting and later backfilled with UHP Ar at a pressure of 90 kPa during fabrication. The cooling rate of suction casting was estimated to be 1000 - 4000℃/s.

The as-casted alloy ingots were cylindrical rods with a diameter of 3 mm. Samples for transmission electron microscopy (TEM) study were transversely cut from the rod to avoid contamination from crucible, followed by mechanical grinding, chemical etching and polishing. The TEM specimens were then irradiated using Intermediate Voltage Electron Microscope (IVEM) facility at Argonne National Laboratory where a Hitachi H-9000NAR microscope was equipped with a TANDEM accelerator. TEM specimens were irradiated with 1 MeV Kr^{++} ions up to 2 dpa (corresponding to a dose of 4×10^{14} ions/cm^2) at room temperature. The beam size was ~ 1.5 mm (without rastering) and was able to cover the entire thin area of TEM specimens during irradiation. A Tecnai F20 transmission electron microscope was operated at an acceleration voltage of 200 keV to examine the microstructure before and after the irradiation experiments. STEM and energy-dispersive X-ray spectroscopy (EDX) analyses were conducted by using high-angle annular dark-field (HADDF) and Oxford detectors attached to the aforementioned TEM microscope.

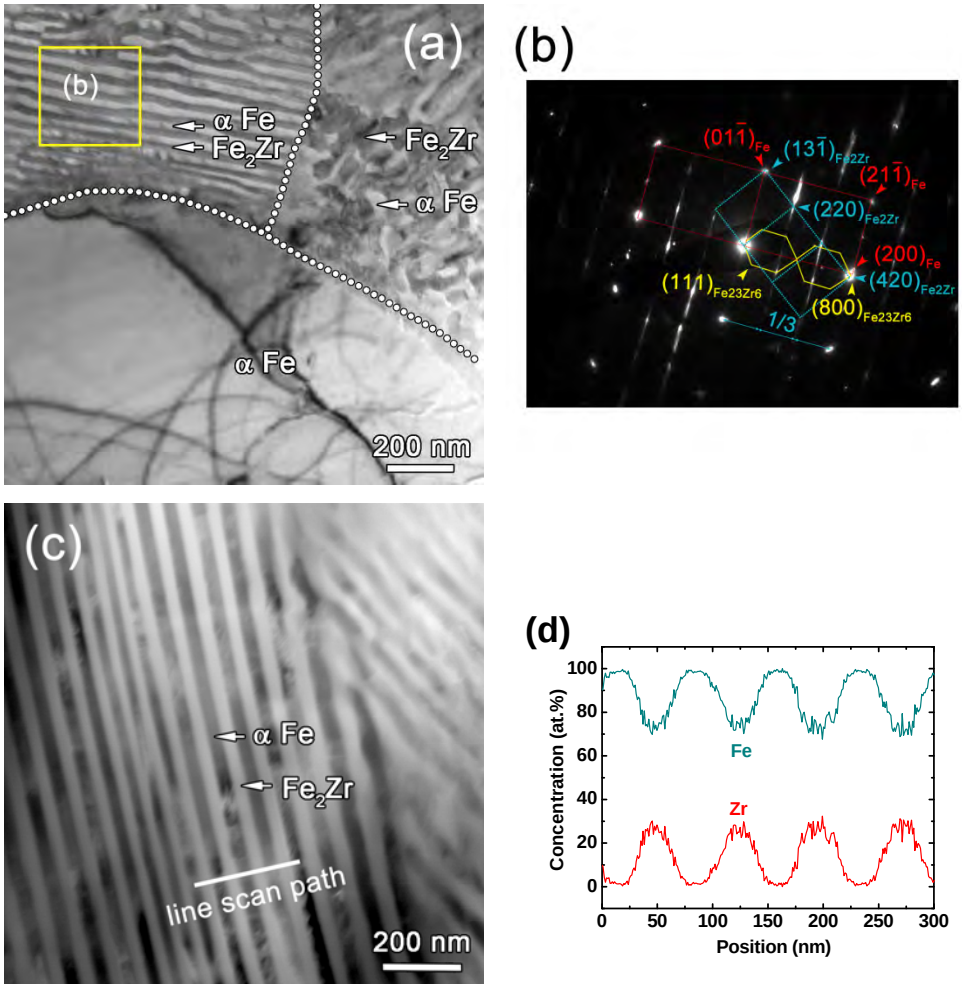

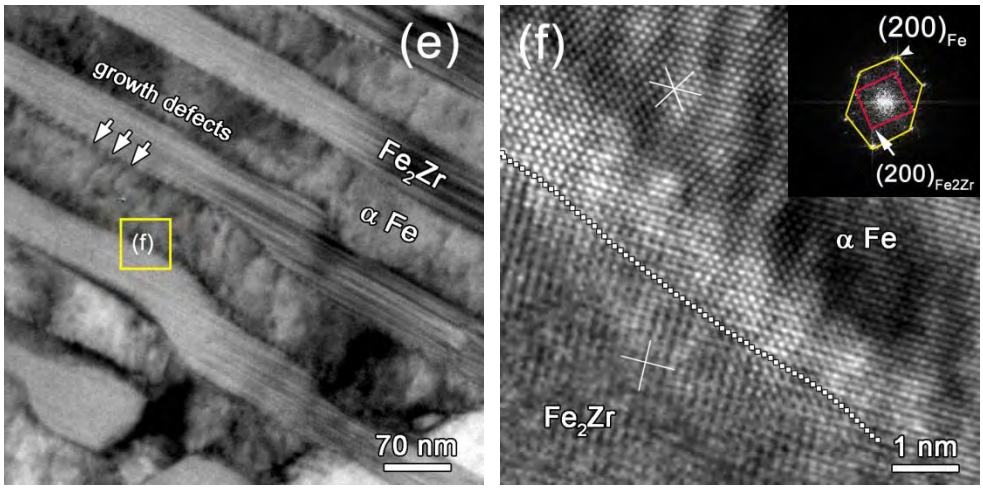

Figure 1. **Microstructure and chemistry of unirradiated α-Fe/Fe_2Zr nanocomposites.** (a) Transmission electron microscopy (TEM) micrograph showing three typical components: large α-Fe grains, cellular and nanolaminate phases consisting of α-Fe and Fe_2Zr layers. (b) The selected area diffraction (SAD) pattern of nanolaminate in box b of Figure 1a shows three sets of diffraction dots, arising from α-Fe, Fe_2Zr and $Fe_{23}Zr_6$ respectively (see supplementary Figure S1 and S2 for more detail), observed from <110> zone axes of bcc α-Fe and fcc-like $Fe_{23}Zr_6$, and <112> zone axis of fcc-like Fe_2Zr. The streaking lines indicate the formation of high density stacking faults in the Fe_2Zr phase. (c) Scanning transmission electron microscopy (STEM) image reveals the laminar α-Fe and Fe_2Zr with average layer thickness of ~ 50 nm. (d) The alternating compositional line profile of nanolaminate determined by energy dispersive X-ray (EDX) spectrum corresponds to α-Fe and Fe_2Zr. (e) Magnified TEM micrograph shows stacking faults in Fe_2Zr layers and growth defects decorating the Fe/Fe_2Zr layer interfaces. (f) High resolution TEM (HRTEM) micrograph reveals incoherent atomic configuration along the Fe/Fe_2Zr layer interface.

As-casted specimens contained three major components: cellular zone, nanolaminates and large α-Fe grains as shown in transmission electron microscopy (TEM) micrograph in Figure 1a. The volume fraction ratio of large grains to eutectic phase is ~ 2 to 1. The selected area diffraction (SAD) pattern of the nanolaminate in the box in Figure 1a shows two major phases: α-Fe (examined from <110> zone axis) and fcc-like Fe_2Zr (C15 type Laves phase with Mg_2Cu as prototype) along <112> zone axis (Figure. 1b), consistent with x-ray diffraction (XRD) profile (Figure S1). $Fe_{23}Zr_6$ is a minor phase as indicated by weak diffraction spots (connected by

orange lines) in Figure 1b. Index of diffraction patterns suggests that α-Fe {200} // $Fe_{23}Zr_6$ {800}. The interplanar spacing of α-Fe {200} nearly equals that of Fe_2Zr {400}, consistent with the lattice parameter ratio of the two phases (a_{Fe} = 0.287 nm, a_{Fe2Zr} = 0.701 nm),[37] and the d-spacing of α-Fe {200} (0.145 nm) is similar to that of $Fe_{23}Zr_6$ {800} (0.15 nm, $a_{Fe23Zr6}$ = 1.172 nm). The streaking lines in Figure 1b indicate the formation of high density stacking faults that are usually observed in the Fe_2Zr phase.[37, 38] Scanning transmission electron microscopy (STEM) image in Figure 1c confirms eutectic nanolaminate structure, and its line-scan compositional profile depicted using energy dispersive X-ray (EDX) spectrum (as shown in Figure 1d) corresponds well to Fe_2Zr and α-Fe. As $Fe_{23}Zr_6$ is a minority phase, we will focus on α-Fe and Fe_2Zr in this irradiation study. Figure 1e shows a magnified TEM micrograph of nanolaminates with high density stacking faults in the Fe_2Zr layers. In addition, growth defects decorating the Fe/Fe_2Zr interfaces were identified. High resolution TEM (HRTEM) micrograph of Fe/Fe_2Zr interface in Figure 1f reveals a typical incoherent configuration of the interface, where α-Fe {200} is nearly parallel to Fe_2Zr {200}, as indicated by the inset fast Fourier transformation (FFT) of the image. Note that the interfacial relationship of Fe/Fe_2Zr varies frequently as shown in Figure S2.

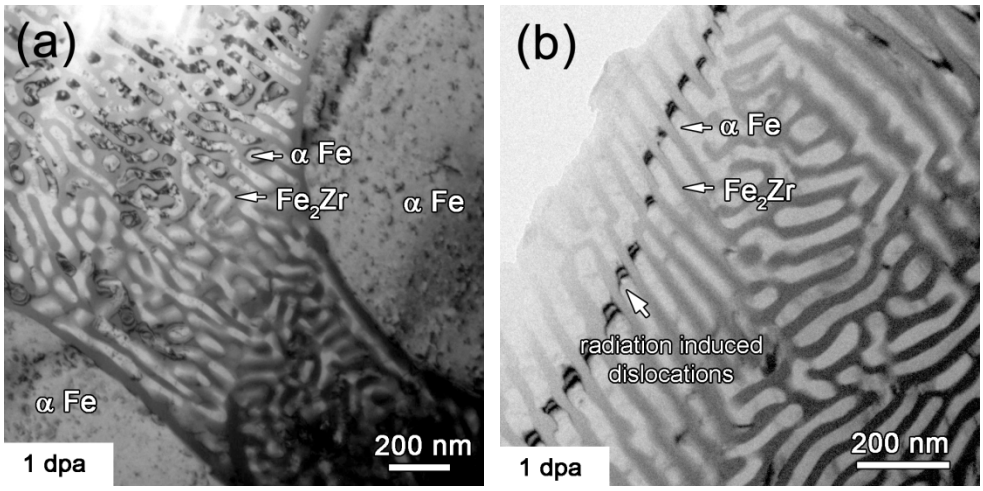

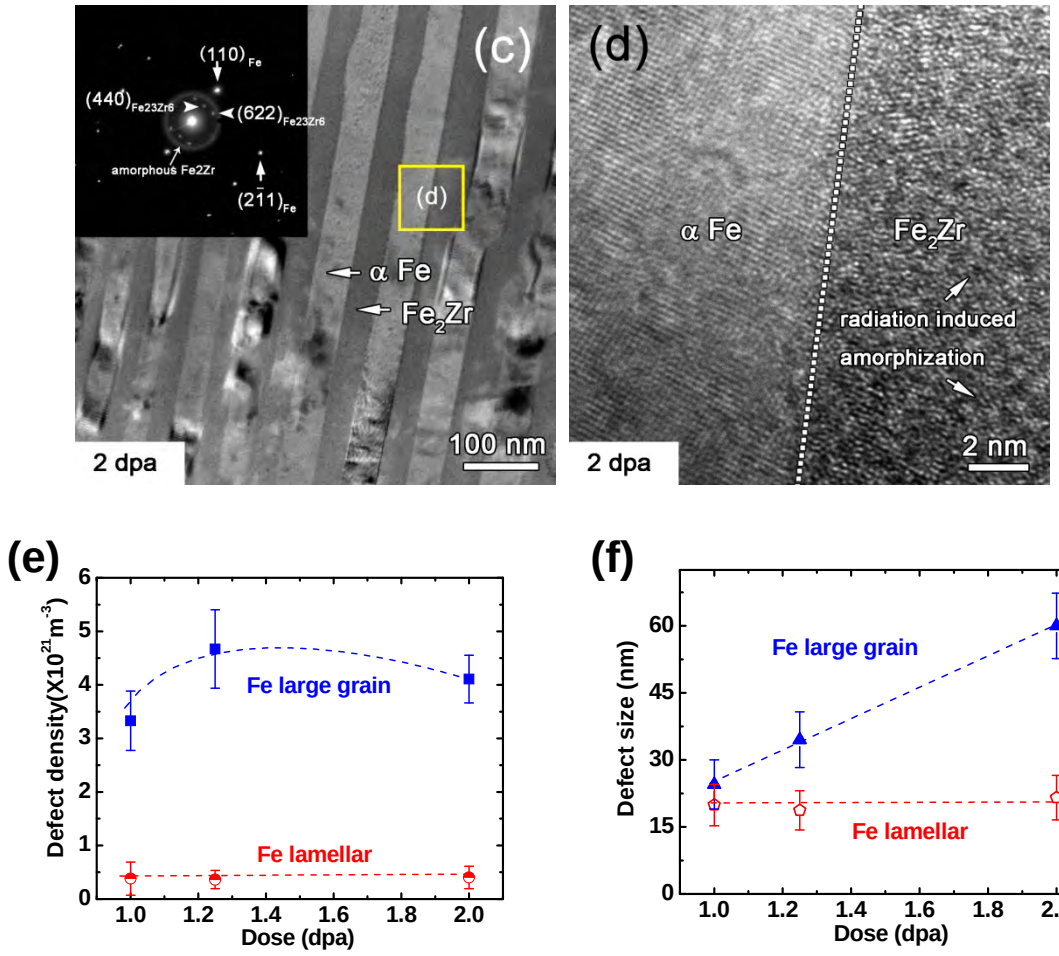

Figure 2. **Microstructure evolution α-Fe/Fe_2Zr nanocomposites subjected to *in situ* Kr ion irradiation up to 2 displacements-per-atom (dpa).** (a) At 1 dpa, TEM micrograph showing abundant defect clusters in the large α-Fe grains. In contrast, smaller defect clusters were observed in cellular areas, residing at the phase boundaries and remained stable during successive irradiation experiments. (b) α-Fe layers in irradiated nanolaminates were mostly clean, with sporadic dislocation loops. Little defect clusters were detected in the irradiated Fe_2Zr layers. (c) At 2 dpa, a TEM micrograph of irradiated nanolaminate revealed the retention of sharp layer interfaces between α-Fe and Fe_2Zr. The halo ring in the inserted SAD pattern reveals the formation of amorphous Fe_2Zr. (d) An HRTEM micrograph along the interface showing amorphization of Fe_2Zr in irradiated nanolaminates. α-Fe remained crystalline structure. **Comparison of dose dependent evolution of defect clusters in α-Fe in large grains and nanolaminates.** (e) Defect density in α-Fe large grains increased rapidly during the initial irradiation, and appeared to reach saturation by ~ 1.25 dpa. In comparison defect density in α-Fe

in nanolaminate was nearly an order of magnitude lower and barely changed up to 2 dpa. (f) In large α-Fe grains, defect size increased monotonically with dose to ~ 60 nm up to 2 dpa, in drastic contrast to nearly unchanged defect dimension of ~ 20 nm in the α-Fe layers in nanolaminates.

In situ irradiation experiments were performed using 1 MeV Kr ions up to a dose of 2 displacements-per-atom (dpa). TEM micrograph of Kr ion irradiated specimen at 1 dpa (Figure 2a) shows abundant defect clusters in large Fe grains. In contrast, much fewer defects were generated in the cellular zones. Irradiated nanolaminates at 1 dpa (Figure 2b) have exceptionally low defect density, despite the sporadically visible dislocation loops bounded in the Fe layers. A magnified TEM image (Figure 2c) of nanolaminates shows defective Fe and clean Fe_2Zr layers. Moreover, the inserted SAD pattern shows a diffuse ring indicating the amorphization of Fe_2Zr. An HRTEM micrograph in Figure 2d shows significant amorphization of Fe_2Zr adjacent to interfaces in nanolaminates (see supplementary Figure S3 for more details).

Statistical studies (in Figure 2e) show that defect density in large Fe grains increased rapidly during the initial stage of irradiation, and appeared to reach saturation by ~ 1.25 dpa, whereas defect density in Fe layers within nanolaminates was much lower and barely varied up to 2 dpa. Meanwhile in large Fe grains, defect size increased monotonically with dose to ~ 60 nm at 2 dpa (Figure 2f), in drastic contrast to nearly unchanged defect dimension of ~ 20 nm in Fe layers in nanolaminate (Figure S4). As defect clusters were absent in irradiated Fe_2Zr layers in nanolaminates, no statistical data were available for comparison for Fe_2Zr layers.

The saturated defect density in the Fe layers of Fe/Fe_2Zr nanolaminates is much lower than that in large Fe grains, implying that a large number of defects must have been annihilated during irradiation. In order to examine the evolution of microstructure of irradiated nanolaminates, we will show two important phenomena captured during *in situ* irradiation studies. The first one is low dose irradiation (less than 0.1 dpa) induced amorphization of Fe_2Zr and subsequent formation of crystal/amorphous interfaces and the second case is a higher dose irradiation initiated dislocation loop migration in Fe layers.

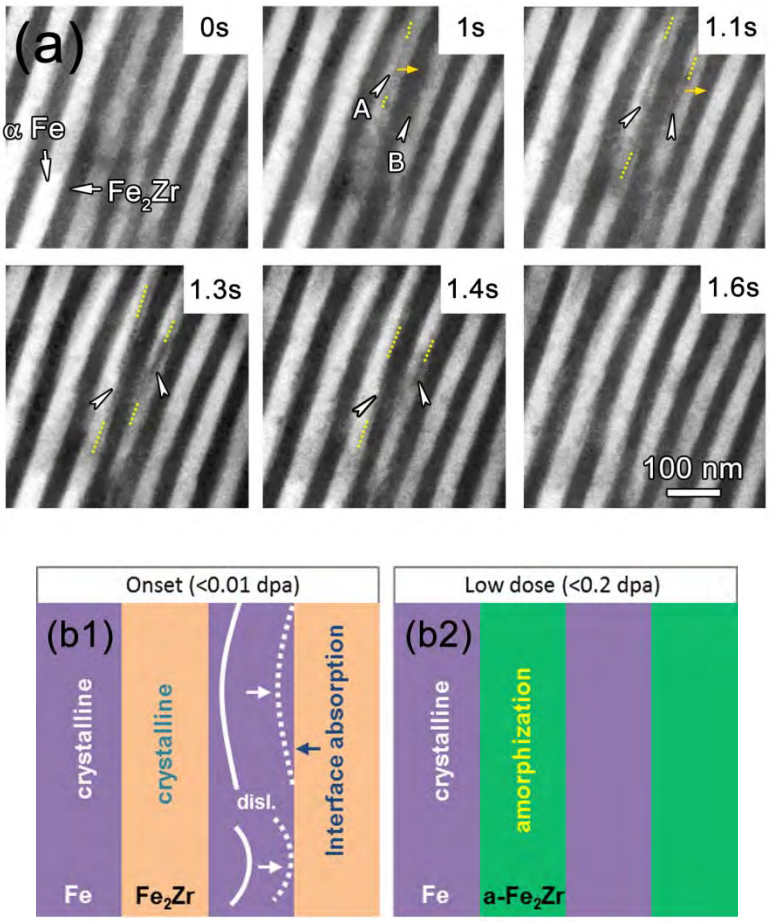

Figure 3. **Defect annihilation by layer interface and amorphization of Fe_2Zr phase in nanolaminates.** (a) *In situ* snapshots of dislocation absorption by Fe/Fe_2Zr layer interface at a dose of about 0.01 dpa (over less than 2 seconds). At 1 s, a dislocation formed in α-Fe layer A and started to evolve and migrate towards the right layer interface, as indicated by the small arrow. The dotted lines mark the ends of the dislocation lines and the small arrows indicate the migration direction. At 1.1 s, the dislocation in layer A became longer and another dislocation line formed in Fe layer B. The two dislocations continued to migrate rightwards at 1.2 and 1.3 s and were absorbed by layer interface at 1.4 s. By 0.2 dpa, Fe_2Zr became nearly amorphous. See Figure S5, Supplementary Video 1 and 2 for more details. (b) Schematics of the "interface-assisted annihilation" mechanism demonstrating the absorption of dislocations by layer interfaces and amorphization of Fe_2Zr at low irradiation dose.

Low dose irradiation induced amorphization of Fe_2Zr and formation of crystal/amorphous interfaces in Fe/Fe_2Zr nanolaminates. Figure 3a shows a series of snapshots of numerous events

of dislocation absorption by Fe/Fe_2Zr layer interface at a low dose (~ 0.01 dpa) (Supplementary Video 1). Before irradiation, crystalline Fe_2Zr layers contained high density stacking faults. At 1 s, a dislocation formed in Fe layer A and started to evolve and migrate towards the right layer interface, as indicated by a small arrow. At 1.1 s, the evolving dislocation became longer and well defined, and nearly reached layer interface. Meanwhile another dislocation line emerged in Fe layer B. The two dislocations continued to migrate rightwards at 1.3 s and the dislocation in layer A were completely absorbed by layer interfaces at 1.4 s, followed by absorption of the dislocation in layer B. Furthermore the crystalline Fe_2Zr layers became amorphous.

Schematics in Figure 3b illustrate the “interface-assisted annihilation” of dislocations and subsequent amorphization of Fe_2Zr. First, irradiation induced dislocation loops in Fe layers evolve into dislocation lines, which propagate towards the Fe/ Fe_2Zr layer interfaces (Figure 3b1). The absorption of dislocations then leads to distortion of crystalline structure in Fe_2Zr layers. Due to the defect absorption and quenching of cascades, amorphization occurs in Fe_2Zr layers (Figure 3b2). Note that irradiation caused immediate destruction of stacking faults in the Fe_2Zr layers, followed by their amorphization at very low dose (< 0.2 dpa). Meanwhile, the layer interface remains stable (chemically abrupt) during the entire irradiation experiments (at higher dose). Post-irradiation analysis also evidenced amorphization (Figure 2) and the absence of stacking faults throughout the irradiated specimen. Another example of low dose irradiation induced defect evolution is shown in Figure S5 and supplementary Video 2. The major reason for the amorphization of Fe_2Zr was the breakage of the chemical bonds induced by heavy ion bombardment. It is likely that the layered structure actively absorbed interstitial atoms (disordering atoms), leaving less possibility for them to recombine (back to order). Therefore, the layered Fe_2Zr might be more vulnerable to radiation induced amorphization in comparision with the bulk one. Please note that the amorphization of Fe_2Zr phase is incomplete at low dose such as 0.01 dpa as shown in Figure 3. It will probably take much higher dose to fully amorphize the Fe_2Zr which we did not observe during our experiments.

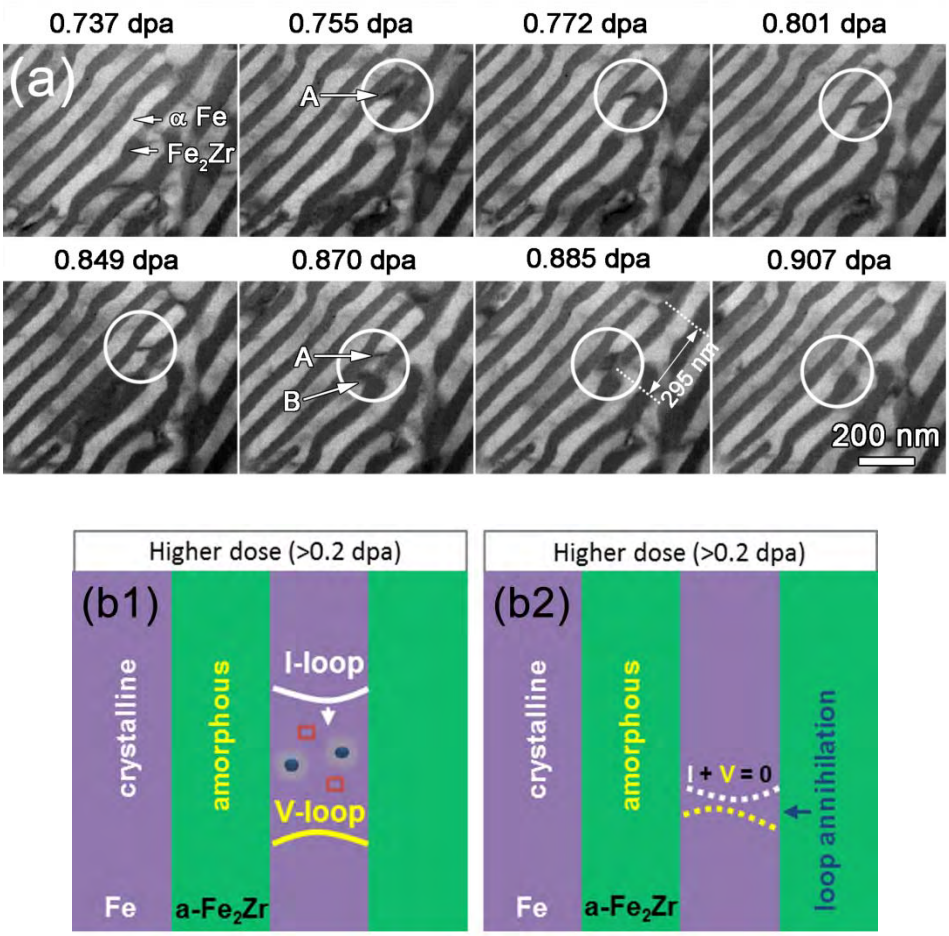

Figure 4. **Annihilation of defect clusters via mobile dislocation loops in confined layers.** (a) *In situ* TEM snapshots of dislocation loop migration over a dose range of 0.737- 0.907 dpa (over 70 s) in confined nanolaminates. At 0.755 dpa, a dislocation loop A was generated and started to migrate downward within the α-Fe layer, as outlined by the circle. Loop A migrated over a distance of 295 nm by 0.885 dpa before it encountered loop B. The two loops then interacted and combined with each other at 0.885 dpa and eventually disappeared at 0.907 dpa. More details as seen in Supplementary Video 3 and 4. (b) Schematics of the defect removal mechanism illustrating the migration of dislocation loops in α-Fe channels and the recombination of dislocation loops with opposite nature. Notice that α-Fe layers are sandwiched between amorphous Fe_2Zr layers.

High dose irradiation induced migration of dislocation loops in Fe layers in nanolaminates (up to 2 dpa). We observed different types of defect morphology in various zones of irradiated

specimens. First, in α-Fe grains, discrete dislocation loops were frequently observed. Many individual loops also combine with one another to form dislocation segments at greater dose. Second, in the cellular zone, defects clusters were often bounded by layer interfaces (Figure 2a). Third, Fe_2Zr nanolayers in nanolaminates were frequently depleted with defect clusters, while defect clusters are typically sporadically distributed in α-Fe layers. And the amorphization of Fe_2Zr nanolayers is widespread in nanolaminates.

Numerous mechanisms could contribute to the drastic reduction of defect cluster density in Fe nanolayers. Misfit dislocations at layer interfaces (Figure 1e-f) may play a role in removing defects. Excess free volume at misfit dislocations can act as sinks to point defects. This mechanism has been proposed to explain size dependent reduction of defect density in Kr ion irradiated Ag/Ni,[25] and He irradiated Cu/Nb,[12] Cu/V[16] and Fe/W[22] multilayers. However, unlike the previously observed rapid migration of defect clusters toward layer interface in Ag/Ni system, we observed, through *in situ* studies, an interesting unexplored mechanism through which defect clusters were removed in α-Fe nanolayers (channels) in nanolaminates with crystal/amorphous layer interfaces.

In situ TEM snap shots in Figure 4a capture one such typical defect annihilation process in Fe nanolayers in nanolaminates. A dislocation loop *A* (outlined in circle in Figure 4a) nucleated at 0.755 dpa and started to migrate (Supplementary Video 3). Loop *A* migrated continuously during subsequent irradiation while another dislocation loop *B* emerged at 0.849 dpa. Loop *A* migrated over a distance of 295 nm before it encountered loop *B* at 0.885 dpa. Subsequently the two loops interacted and annihilated each other at 0.907 dpa.

The mechanism of such a defect annihilation mechanism is shown schematically in Figure 4b. First, defect clusters in Fe layers can evolve into a larger dislocation loop confined by crystal/amorphous layer interfaces. Mobile dislocation loops can migrate over hundreds of nm in long narrow α-Fe layers (channels), wherein point defects of the same (opposite) nature are collected or removed (Figure 4b1). Meanwhile such mobile interstitial loops may eventually encounter and annihilate vacancy loops in the channel (Figure 4b2). Thus these mobile interstitial loops could act as “sweeper” in Fe layer to wipe out most other immobile defect clusters before they are annihilated by loops with opposite Burgers vector. In contrast in large α-Fe grains, the dimension and density of defect clusters increase monotonically with dose as there is insufficient defect sinks to absorb these defects. In the cellular zones, the defects are

bounded by limited layer interfaces with insufficient capability (or low probability) to nucleate mobile dislocation loops.

The role of amorphous Fe_2Zr nanolayers is critical. First, the amorphous layers have abundant excess free volumes, which can accommodate the large number of irradiation induced point defects in α-Fe. Second, such amorphous layers are not transparent to mobile dislocations loops. The mobile dislocation loops generated in confined α-Fe channels can thus propagate frequently to collect and remove other type of irradiation induced defect clusters. Third, the crystal/amorphous interface is resistant to irradiation induced intermixing up to at least 2 dpa, even though the adjacent layers include identical elements (Fe). Fourth, the amorphous Fe_2Zr interface curtails the growth of defect clusters in irradiated Fe layers.

In summary, rapidly solidified bulk $Fe_{96}Zr_4$ nanocomposite consists of Fe/Fe_2Zr nanolaminates, cellular zones and large Fe grains. Irradiated nanolaminates contained much lower defect density and smaller defect size than those in large Fe grains. Low dose irradiation induced amorphization of Fe_2Zr and the crystal/amorphous layer interfaces absorbed irradiation induced defects and lead to confinement of defect clusters. *In situ* video evidenced active defect annihilation due to the sweeping effect of mobile dislocation loops confined in Fe nanolayers. This study provides an encouraging outlook on the implementation of crystal/amorphous interfaces in the design of bulk irradiation tolerant nanocomposites for extreme irradiation environments.

Reference

[1] Grimes RW, Konings RJ, Edwards L. Greater tolerance for nuclear materials. Nature materials. 2008; 7.
[2] Zinkle SJ, Busby JT. Structural materials for fission & fusion energy. Materials Today. 2009; 12: 12-19.
[3] Zinkle SJ, Was GS. Materials challenges in nuclear energy. Acta Materialia. 2013; 61: 735-758.
[4] Sickafus KE, Grimes RW, Valdez JA, Cleave A, Tang M, Ishimaru M, Corish SM, Stanek CR, Uberuaga BP. Radiation-induced amorphization resistance and radiation tolerance in structurally related oxides. Nature materials. 2007; 6: 217-223.
[5] Odette GR, Alinger MJ, Wirth BD. Recent Developments in Irradiation-Resistant Steels. Annual Review of Materials Research. 2008; 38: 471-503.
[6] Misra A, Verdier M, Lu YC, Kung H, Mitchell TE, Nastasi M, Embury JD. Structure and mechanical properties of Cu-X (X = Nb,Cr,Ni) nanolayered composites. Scripta Materialia. 1998; 39: 555-560.
[7] Anderson P, Li C. Hall-Petch relations for multilayered materials. Nanostructured Materials. 1995; 5: 349-362.
[8] Hoagland R, Mitchell T, Hirth J, Kung H. On the strengthening effects of interfaces in multilayer fee metallic composites. Philosophical Magazine A. 2002; 82: 643-664.
[9] Zhang X, Misra A, Wang H, Shen T, Nastasi M, Mitchell T, Hirth J, Hoagland R, Embury J. Enhanced hardening in Cu/330 stainless steel multilayers by nanoscale twinning. Acta Materialia. 2004; 52: 995-1002.
[10] Zhang JY, Liu Y, Chen J, Chen Y, Liu G, Zhang X, Sun J. Mechanical properties of crystalline Cu/Zr and crystal–amorphous Cu/Cu–Zr multilayers. Materials Science and Engineering: A. 2012; 552: 392-398.

[11] Zhang X, Li N, Anderoglu O, Wang H, Swadener JG, Höchbauer T, Misra A, Hoagland RG. Nanostructured Cu/Nb multilayers subjected to helium ion-irradiation. Nuclear Instruments and Methods in Physics Research Section B: Beam Interactions with Materials and Atoms. 2007; 261: 1129-1132.
[12] Zhang X, Fu E, Li N, Misra A, Wang Y-Q, Shao L, Wang H. Design of Radiation Tolerant Nanostructured Metallic Multilayers. Journal of Engineering Materials and Technology. 2012; 134: 041010.
[13] Misra A, Demkowicz M, Zhang X, Hoagland R. The radiation damage tolerance of ultra-high strength nanolayered composites. JOM Journal of the Minerals, Metals and Materials Society. 2007; 59: 62-65.
[14] Fu EG, Misra A, Wang H, Shao L, Zhang X. Interface enabled defects reduction in helium ion irradiated Cu/V nanolayers. Journal of Nuclear Materials. 2010; 407: 178-188.
[15] Fu EG, Wang H, Carter J, Shao L, Wang YQ, Zhang X. Fluence-dependent radiation damage in helium (He) ion-irradiated Cu/V multilayers. Philosophical Magazine. 2012; 93: 883-898.
[16] Fu EG, Carter J, Swadener G, Misra A, Shao L, Wang H, Zhang X. Size dependent enhancement of helium ion irradiation tolerance in sputtered Cu/V nanolaminates. Journal of Nuclear Materials. 2009; 385: 629-632.
[17] Yuan W. Helium effects on the stability of the interface of Cu/W nanomultilayers. Acta Phys. Sin. 2012; 61.
[18] Li N, Carter JJ, Misra A, Shao L, Wang H, Zhang X. The influence of interfaces on the formation of bubbles in He-ion-irradiated Cu/Mo nanolayers. Philosophical Magazine Letters. 2010; 91: 18-28.
[19] Yu KY, Liu Y, Fu EG, Wang YQ, Myers MT, Wang H, Shao L, Zhang X. Comparisons of radiation damage in He ion and proton irradiated immiscible Ag/Ni nanolayers. Journal of Nuclear Materials. 2013; 440: 310-318.
[20] Wei QM, Li N, Mara N, Nastasi M, Misra A. Suppression of irradiation hardening in nanoscale V/Ag multilayers. Acta Materialia. 2011; 59: 6331-6340.
[21] Li N, Martin MS, Anderoglu O, Misra A, Shao L, Wang H, Zhang X. He ion irradiation damage in Al/Nb multilayers. Journal of Applied Physics. 2009; 105: 123522-123528.
[22] Li N, Fu EG, Wang H, Carter JJ, Shao L, Maloy SA, Misra A, Zhang X. He ion irradiation damage in Fe/W nanolayer films. Journal of Nuclear Materials. 2009; 389: 233-238.
[23] Demkowicz MJ, Bellon P, Wirth BD. Atomic-scale design of radiation-tolerant nanocomposites. MRS Bulletin. 2010; 35: 992-998.
[24] Zhang X, Fu EG, Misra A, Demkowicz MJ. Interface-enabled defect reduction in He ion irradiated metallic multilayers. JOM. 2010; 62: 75-78.
[25] Yu KY, Sun C, Chen Y, Liu Y, Wang H, Kirk MA, Li M, Zhang X. Superior tolerance of Ag/Ni multilayers against Kr ion irradiation: an in situ study. Philosophical Magazine. 2013; 93: 3547-3562.
[26] Xu W, Zhang Y, Cheng G, Jian W, Millett PC, Koch CC, Mathaudhu SN, Zhu Y. In-situ atomic-scale observation of irradiation-induced void formation. Nature communications. 2013; 4.
[27] Kaoumi D, Motta AT, Birtcher RC. A thermal spike model of grain growth under irradiation. Journal of Applied Physics. 2008; 104: 073525.
[28] Sun C, Song M, Yu K, Chen Y, Kirk M, Li M, Wang H, Zhang X. In situ Evidence of Defect Cluster Absorption by Grain Boundaries in Kr Ion Irradiated Nanocrystalline Ni. Metallurgical and Materials Transactions A. 2013; 1-9.
[29] Yu KY, Bufford D, Sun C, Liu Y, Wang H, Kirk MA, Li M, Zhang X. Removal of stacking-fault tetrahedra by twin boundaries in nanotwinned metals. Nat Commun. 2013; 4: 1377.
[30] Yu KY, Bufford D, Khatkhatay F, Wang H, Kirk MA, Zhang X. In situ studies of irradiation-induced twin boundary migration in nanotwinned Ag. Scripta Materialia. 2013; 69: 385-388.
[31] Sun C, Bufford D, Chen Y, Kirk M, Wang Y, Li M, Wang H, Maloy S, Zhang X. In situ study of defect migration kinetics in nanoporous Ag with enhanced radiation tolerance. Scientific reports. 2014; 4.
[32] Fu EG, Caro M, Zepeda-Ruiz LA, Wang YQ, Baldwin K, Bringa E, Nastasi M, Caro A. Surface effects on the radiation response of nanoporous Au foams. Applied Physics Letters. 2012; 101.
[33] Bringa EM, Monk JD, Caro A, Misra A, Zepeda-Ruiz L, Duchaineau M, Abraham F, Nastasi M, Picraux ST, Wang YQ, Farkas D. Are Nanoporous Materials Radiation Resistant? Nano Letters. 2011; 12: 3351-3355.
[34] Kiener D, Hosemann P, Maloy S, Minor A. In situ nanocompression testing of irradiated copper. Nature materials. 2011; 10: 608-613.
[35] Landau P, Guo Q, Hattar K, Greer JR. The Effect of He Implantation on the Tensile Properties and Microstructure of Cu/Fe Nano-Bicrystals. Advanced Functional Materials. 2013; 23: 1281-1288.
[36] Han W, Demkowicz MJ, Mara NA, Fu E, Sinha S, Rollett AD, Wang Y, Carpenter JS, Beyerlein IJ, Misra A. Design of Radiation Tolerant Materials Via Interface Engineering. Advanced Materials. 2013; 25: 6975-6979.
[37] Stein F, Sauthoff G, Palm M. Experimental determination of intermetallic phases, phase equilibria, and invariant reaction temperatures in the Fe-Zr system. Journal of Phase Equilibria. 2002; 23: 480-494.
[38] Liu Y, Livingston JD, Allen SM. Room-temperature deformation and stress-induced phase. Metallurgical Transactions A. 1992; 23: 3303-3308.

4. Administrative actions

The project has supported the research of the following personnel.

Name	**Title**
Xinghang Zhang	PI, Associate professor
Kaiyuan Yu	Graduate student (2009-2013); Postdoctoral fellow (2013-2014);
Youxing Chen	Graduate student (2010 - present)
Zhe Fan	Graduate student (started in fall 2012)

5. Near term plans

We plan to perform the following tasks by using the instrumentation.

1) Fabricate bulk nanostructured metals
2) Fabricate bulk metals with the incorporation of oxide nanoparticles
3) Perform mechanical testing on the fabricated bulk nanostructured alloys.